ADVANCED FUNCTIONAL MATERIALS
www.afm-journal.de

Spinel-Structured High-Entropy Oxide Nanofibers as Electrocatalysts for Oxygen Evolution in Alkaline Solution: Effect of Metal Combination and Calcination Temperature

Claudia Triolo, Kaveh Moulaee, Alessandro Ponti, Gioele Pagot, Vito Di Noto, Nicola Pinna, Giovanni Neri, and Saveria Santangelo**

Defect-engineering is a viable strategy to improve the activity of nanocatalysts for the oxygen evolution reaction (OER), whose slow kinetics still strongly limits the broad market penetration of electrochemical water splitting as a sustainable technology for large-scale hydrogen production. High-entropy spinel oxides (HESOs) are in focus due to their great potential as low-cost OER electrocatalysts. In this work, electrospun HESO nanofibers (NFs), based on (Cr,Mn,Fe,Co,Ni), (Cr,Mn,Fe,Co,Zn) and (Cr,Mn,Fe,Ni,Zn) combinations, with granular architecture and oxygen-deficient surface are produced by calcination at low temperature (600 or 500 °C), characterized by a combination of benchtop analytical techniques and evaluated as electrocatalysts for OER in alkaline medium. The variation of HESO composition and calcination temperature produces complex and interdependent changes in the morphology of the fibers, crystallinity and inversion degree of the spinel oxide, concentration of the oxygen-vacancies, cation distribution in the lattice, which mirror on different electrochemical properties of the fibers. The best electrocatalytic performance (overpotential and Tafel slope at 10 mA cm^{-2}: 360 mV and 41 mV dec^{-1}, respectively) pertains to $(Cr_{1/5}Mn_{1/5}Fe_{1/5}Co_{1/5}Ni_{1/5})_3O_4$ NFs calcined at 500 °C and results from the lower outer 3d-electron number, e_g filling closer to its optimal value and higher occupation of 16*d* sites by the most redox-active species.

1. Introduction

Clean energy is still a pressing concern for human society today. Meeting the growing global energy demand in an environmentally-benign manner is essential to our planet's future. Nowadays, fossil fuels are the primary source of energy, but these resources are limited, and their continued use can have negative effects on the environment, more pronounced in recent decades due to the growing need for energy. Therefore, it is necessary to develop alternative sources of sustainable energy. In recent years, hydrogen has attracted enormous interest, as it can be used in various industrial fields, such as oil refining and metal treatment, in the production of fertilizers (ammonia) and in food processing,[1] and it is a promising alternative energy source.

There are various physical and chemical processes that can produce hydrogen.[2] Among them, electrochemical water splitting (WS) has attracted much attention for its effectiveness in large-scale hydrogen

C. Triolo, S. Santangelo
Dipartimento di Ingegneria Civile
dell'Energia
dell'Ambiente e dei Materiali (DICEAM)
Università "Mediterranea"
Via Zehender, Loc. Feo di Vito, Reggio Calabria 89122, Italy
E-mail: saveria.santangelo@unirc.it

C. Triolo, S. Santangelo
National Reference Center for Electrochemical Energy Storage (GISEL)
Consorzio Interuniversitario Nazionale per la Scienza e Tecnologia dei Materiali (INSTM)
Firenze 50121, Italy

The ORCID identification number(s) for the author(s) of this article can be found under https://doi.org/10.1002/adfm.202306375

DOI: 10.1002/adfm.202306375

K. Moulaee, G. Neri
Dipartimento di Ingegneria
Università di Messina
Contrada di Dio, Vill. Sant'Agata, Messina 98166, Italy
E-mail: gneri@unime.it

A. Ponti
Laboratorio di Nanotecnologie
Istituto di Scienze e Tecnologie Chimiche "Giulio Natta" (SCITEC)
Consiglio Nazionale delle Ricerche
Via Fantoli 16/15, Milano 20138, Italy

G. Pagot, V. Di Noto
Section of Chemistry for the Technology (ChemTech)
Department of Industrial Engineering
University of Padova
Via Marzolo 9, Padova (PD) 35131, Italy

N. Pinna
Department of Chemistry
IRIS Adlershof & The Center for the Science of Materials Berlin
Humboldt-Universität zu Berlin
Brook-Taylor-Str. 2, 12489 Berlin, Germany

production.[3] Two half-reactions occur in water electrolysis, the oxygen evolution reaction (OER) at the anode and the hydrogen evolution reaction (HER) at the cathode. Ideally, under standard conditions, electrochemical WS requires a thermodynamic potential of 1.23 V, corresponding to an energy of 237.1 kJ mol^{-1}. However, since overpotentials are required for generating sufficient current density due to the slow kinetics of the two reactions, the energy conversion efficiency is relatively low. An electrocatalyst capable of accelerating the reaction rate by reducing overpotential is highly desirable to counteract slow kinetics and bypass complex multi-electron reaction pathways.[4] Catalysts commonly utilized in both HER and OER are expensive since they contain noble metals (mainly Ir, Ru and Pt).[5,6] Developing new catalytic materials, cheaper and/or more active toward OER and HER, is the way to overcome this problem. Several efforts have been devoted to achieving this goal.[7–16] Moreover, electrochemical WS of seawater is gaining attention as a long-term sustainable solution for the large-scale application of WS,[17–20] which would be problematic in many regions of the world as it needs large quantities of high-purity water.

OER is considered the bottleneck of the WS process as it is the major source of energy loss. Hence, the development of highly-performing, noble-metal-free catalysts for OER is particularly rewarding. Earth-abundant and non-precious transition metal (TM) oxides are in focus due to the great potential resulting from their activity, stability, and low cost.[9,21] Inkjet printing is one of the most attractive additive technologies for the electrode manufacturing in electrocatalysis.[22] Very recently, it has been suggested that electrospun oxide nanofibers (NFs) with granular architecture can have great potential as ink-jet printable electrocatalysts, thanks to the possibility of easily separating the nanograins that make up the fibers from each other.[23] Among them, spinel-structured high-entropy oxide (HESO) NFs, benefiting from the synergy among their multiple-metallic components,[24] have been shown to be promising candidates as alternative to expensive noble-metal-based catalysts for OER in alkaline electrolyte.[12] Based on the current assessments on spinel-type OER electrocatalysts,[25,26] it has been proposed that the occupation of octahedral sites by redox-active centers and oxygen vacancies (OVs) are mostly responsible for their good electrochemical performance.[23] The transformation from tetrahedral to octahedral coordinated cation introduces OVs and coordinately unsaturated metal octahedra MO_{6-x}.[27] MO_{6-x} units on the surface are the active centers for the OER.[27]

Higher occupation of octahedral sites by redox-active metal centers and greater covalence of the metal-oxygen redox building blocks can be achieved by engineering the HESO composition,[25,26,28] whereas the concentration of OVs, which, in electrospun oxide NFs, are located at nanograin fusion interfaces, can be increased by enhancing the grain boundary (GB) density through the change of the calcination temperature.[29]

Actually, defect engineering has recently emerged as a viable strategy to improve the electrocatalytic performance of nanomaterials.[21,30–35] Defective high-entropy rock-salt (Mg,Co,Ni,Cu,Zn) oxide prepared by electrospinning, Ar-annealing and air-calcination at 1000°C exhibits high stability (25 h) and lower Tafel slope (61.4 mV dec^{-1}) than common low-entropy nickel and cobalt oxide (NiO and CoO) catalysts.[31] Greater stability (60 h) and faster kinetics (Tafel slope: 50.3 mV dec^{-1}) have been reported for nanoporous spinel-type high-entropy (Cr,Mn,Fe,Co,Ni) oxide with high GB density, obtained by low temperature solution combustion.[32]

This work focuses on the preparation of OV-rich spinel-type electrospun HESO NFs to be used as electrocatalysts for OER in alkaline medium. The rationale is to improve their electrochemical properties through the increase of the OV-concentration and the occupation of octahedral sites by redox-active cations, while simultaneously mitigating the environmental impact of their production process. For this purpose, *i*) three different equimolar metal combinations (MCs) are considered, namely (Cr,Mn,Fe,Co,Ni), (Cr,Mn,Fe,Co,Zn) and (Cr,Mn,Fe,Ni,Zn), and *ii*) for each combination, calcination is carried out at low temperature (600 or 500 °C) to obtain NFs constituted by fine oxide grains and, thus, with high density of GBs. The aim of the work is to study the complex and interdependent changes induced by the variation of HESO composition and calcination temperature on the morphology of the fibers, crystallinity and inversion degree of the spinel oxide, density of the GBs and concentration of the OVs, cation distribution in the lattice and the effects that they produce on the electrocatalytic behavior of the fibers.

For easy identification, in the following the HESO-electrocatalysts are labelled as the varying cations in the five MCs (**Table 1**), namely CoNi-T_C, CoZn-T_C and NiZn-T_C, with T_C indicating the calcination temperature expressed in °C.

2. Results and Discussion

2.1. Physicochemical Properties

The morphology, texture, elemental distribution, microstructure, crystalline phase, and surface composition of the produced materials were investigated by scanning electron microscopy (SEM), high-resolution transmission electron microscopy (HRTEM), high-angle annular dark-field scanning transmission electron microscopy (HAADF-STEM), energy-dispersive X-ray spectroscopy (EDX) x-ray diffraction (XRD), micro-Raman spectroscopy (MRS) and x-ray photoelectron spectroscopy (XPS).

Figure 1, Figures S2 and S3 (Supporting Information) summarize the results of the SEM/EDX analyses. SEM images (Figure 1a–f) demonstrate that, regardless of the MC, (Cr,Mn,Fe,Co,Ni), (Cr,Mn,Fe,Co,Zn) or (Cr,Mn,Fe,Ni,Zn), and T_C, 500 or 600°C, micrometer-long NFs are formed upon heating treatment from the as-spun polymer/metal-salts 1D templates. For any composition, fibers calcined at 500 °C appear longer and thicker than those calcined at 600°C (Figure S2, Supporting Information). At given T_C, the center value of the NF diameter distribution increases in the order CoZn < NiZn < CoNi (Figure 1g). EDX analysis (Figure S3, Supporting Information) proves the spatially uniform distribution of metals and oxygen throughout all samples at the micro-scale.

TEM imaging (**Figure 2**a–l; Figure S4, Supporting Information) reveals that all fibers exhibit the granular structure peculiar to electrospun oxides.[29,36–40] They consist of densely packed polyhedron-shaped oxide grains with sizes ranging from about ten nm to a few tens of nm, depending on both T_C and MC (Figure 2g–l) During calcination, the degradation of organic components of the hybrid PAN/acetates fibers causes

Table 1. Metal combinations, calcination temperature (T_C) and sample codes. The phase of the HESO formed is also reported.

Metal combination						T_C/°C	Code	Oxide phase
Cr	Mn	Fe	Co	Ni		500	CoNi-500	$(Cr_{1/5}Mn_{1/5}Fe_{1/5}Co_{1/5}Ni_{1/5})_3O_4$
						600	CoNi-600	
Cr	Mn	Fe	Co		Zn	500	CoZn-500	$(Cr_{1/5}Mn_{1/5}Fe_{1/5}Co_{1/5}Zn_{1/5})_3O_4$
						600	CoZn-600	
Cr	Mn	Fe		Ni	Zn	500	NiZn-500	$(Cr_{1/5}Mn_{1/5}Fe_{1/5}Ni_{1/5}Zn_{1/5})_3O_4$
						600	NiZn-600	

PAN and embedded acetates to experience opposite solicitations (expansion outwards and contraction inwards, respectively[30,31]) resulting in the formation of space-confined, defect-rich oxide grains, interconnected to each other to build a porous 1D architecture.

The large surface area and porous nature of the resulting fibers translates into high accessibility for the electrolyte and large number of exposed sites, which is beneficial for the OER reaction. As expected,[29,41] for a given MC, the nanograins forming the fibers calcined at 500 °C are, on average, smaller in size than those which compose the fibers treated at 600 °C, as well as those produced at higher temperature (900 °C), subject of previous studies.[23,28]

STEM/EDX elemental maps (Figure 2m–p; Figure S5a–h, Supporting Information) proves the spatially uniform distribution of the metal ions throughout all samples at the nano-scale. Additional information on the NF morphology was inferred by carrying out projection analysis of STEM-EDX maps.[28] The results (Figure S5i–t, Supporting Information) confirm the homogeneous distribution of metal ions and show that, CoNi and NiZn NFs calcined at 500 °C display a substantially solid morphology, whereas CoZn-500 NFs are quasi hollow. In NiZn-600

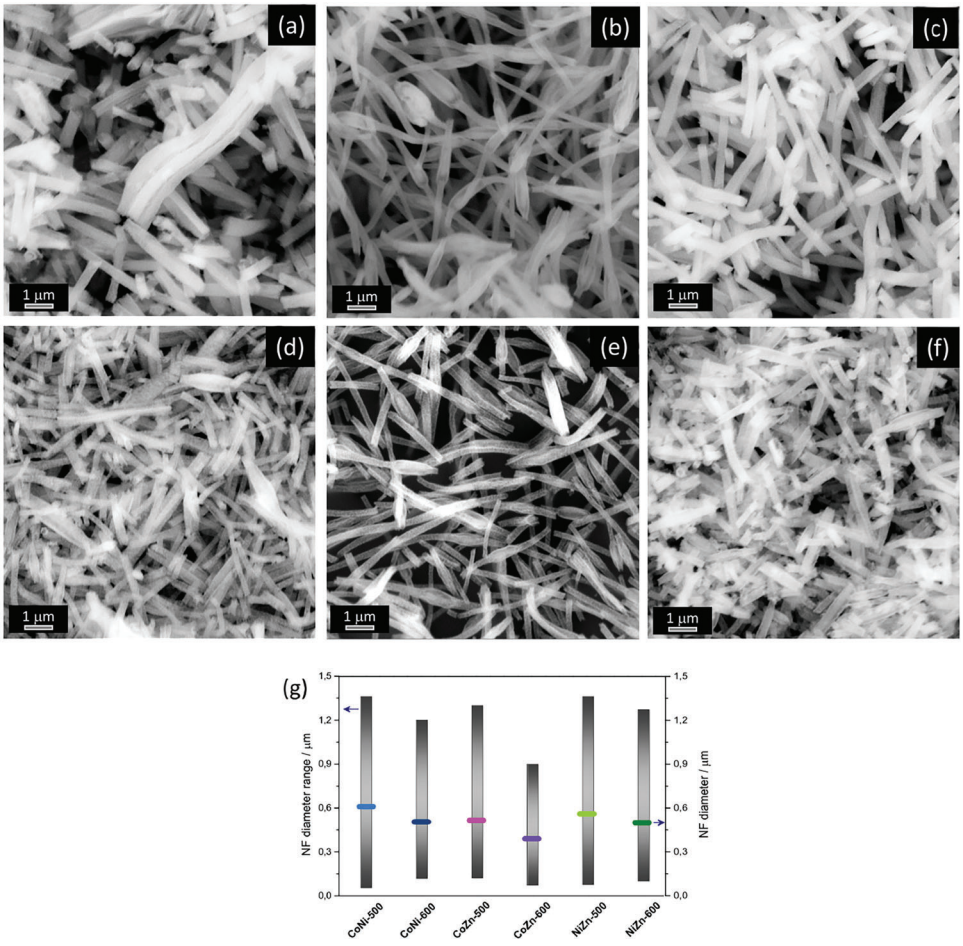

Figure 1. a–f) Morphology of the electrospun NFs, as resulting from the SEM analysis (the shown micrographs refer to samples a) CoNi-500, b) CoZn-500, c) NiZn-500, d) CoNi-600, e) CoZn-600 and f) NiZn-600). g) NF diameter ranges and center values of the NF diameter distributions.

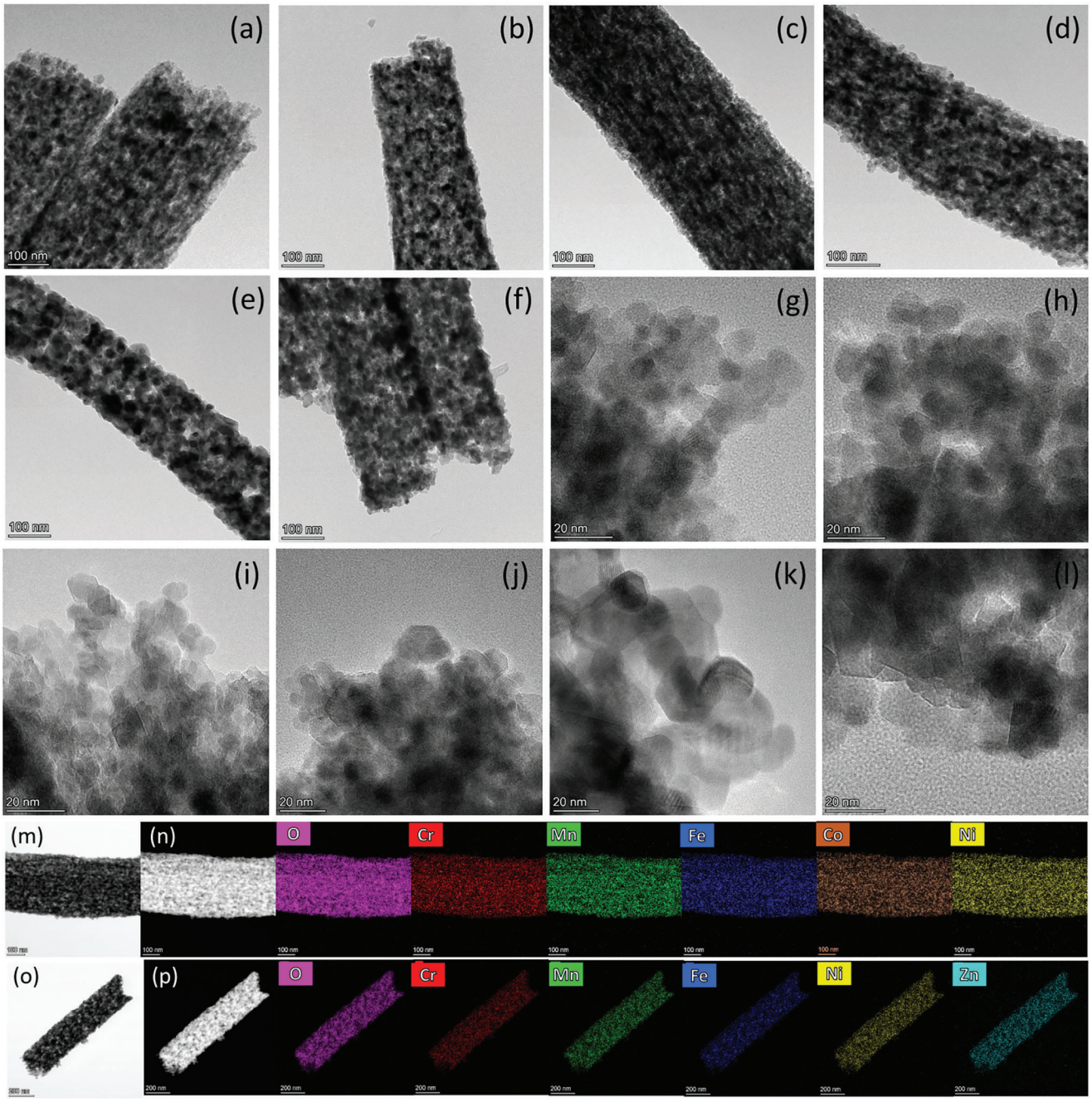

Figure 2. a–p) TEM images of electrospun NFs a,g) CoNi-500, b,h) CoZn-500, c,i) NiZn-500, d,j) CoNi-600, e,k) CoZn-600 and f,l) NiZn-600. m,o) BF-STEM and n,p) HAADF-STEM images of m,n) CoNi-500 and o,p) NiZn-600, followed by the elemental maps.

NFs, some cavity along the NF axis begins to develop, while upon calcination at 600 °C CoZn NFs become hollow. NFs with hollow-tube architecture had been previously obtained by calcination at 900 °C.[23,28] These findings are consistent with reports on the evolution of fiber microstructure produced by variation in T_C.[29]The increase of T_C causes the specific surface area to decrease[42] as the development of larger grains at expenses of the smaller ones is promoted, with reduction in the grain density and fusion areas,[29] due to the tendency to minimize the interfacial surface energy.[43] At given T_C, the size of the nanograins increases in the order NiZn < CoNi < CoZn.

The presence of lattice fringes in HR-TEM images of the NFs shows that grains are crystalline. In most cases, the grains at the NF edge or tip are single crystals with size 10–30 nm; very few polycrystalline grains are observed. Geometrical phase analysis (GPA, **Figure 3**) of lattice fringes reveals that some lattice strain is present in most grains, but strain is not related to the location of the grain.

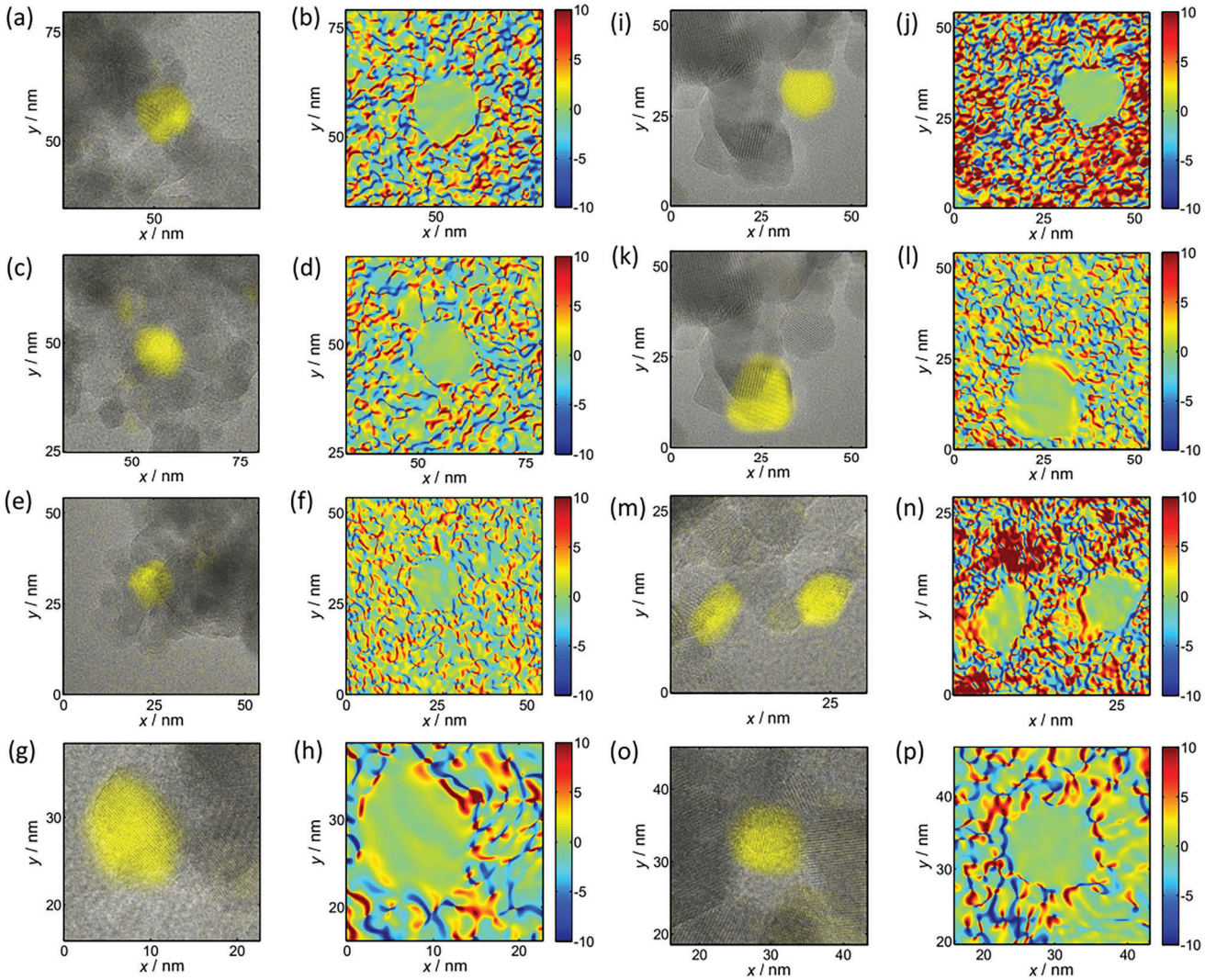

Figure 3. Geometrical phase analysis of the NFs. a,c,e,g,l,k,m,o) Intensity-colorized HR-TEM images and b,d,f,h,j,l,n,p) lattice strain maps (% cell size). The shown images refer to NFs a–d) CoNi-500, e,f) CoNi-600, g,h) CoZn-500, i–l) CoZn-600, m,n) NiZn-500, and o,p) NiZn-600. Crystallites in the shown CoNi-500 NF have similar strain pattern, weak strain extended to the whole crystallite and heavy elongation strain where they touch other crystallites, despite they are located a,b) at the very edge of the NF ([220] fringes) and c,d) well within the NF ([222] fringes). The latter is similar to the crystallites in e,f) CoNi-600 NF ([111] fringes) and (p,o) NiZn-600 ([220] fringes); the former to the CoZn-500 crystallite ([220] fringes) in g,h). Only one of the two crystallites ([111] and [311] fringes) at the very edge of i–l) CoZn-600 NF displays prominent extended strain, while the two crystallites in m,n) NiZn-500 NF (both [111] fringes, lattices form ≈5° angle) show heavy strain.

To investigate the lattice orientation of the crystallites from the HR-TEM images, a new image representation was introduced where all crystallites with the *same fringe period* in an image are shown as colored patches with hue denoting the orientation of the crystal lattice reciprocal vector corresponding to the fringe period in the image plane (**Figure 4**). No obvious geometric lattice relationships was observed between neighboring crystallites in any NF sample, as particularly evident when comparing the maps for the different reciprocal vectors in the same region of a CoZn-600 NF.

In full agreement with information inferred from the selected-area electron diffraction (SAED) patterns (Figure S4m–r, Supporting Information), regardless of T_C, all reflections detected in the diffractograms of the NFs (**Figure 5**a) can be indexed to the spinel structure (JCPDS no. 22–1084).[44–50] Rietveld refinements from XRD data (Figure S6, Supporting Information) confirm the absence of secondary phase(s) and the formation of pure single-phase spinel. Starting from the same precursor spinnable solutions, single-phase high-entropy (Cr,Mn,Fe,Co,Ni), (Cr,Mn,Fe,Co,Zn) and (Cr,Mn,Fe,Ni,Zn) oxide NFs with spinel structure had been previously obtained by calcination at higher temperature.[23,28] This finding fully agrees with the existence of a wide temperature range for the formation of a single spinel-phase, reported by Sun et al.[51]

In the XRD patterns of the fibers calcined at 600 °C, peaks are sharper than in those of the fibers calcined at 500 °C, proving that the change in T_C affects not only the microstructure of the fibers, but also the crystallinity of the oxide nanograins.

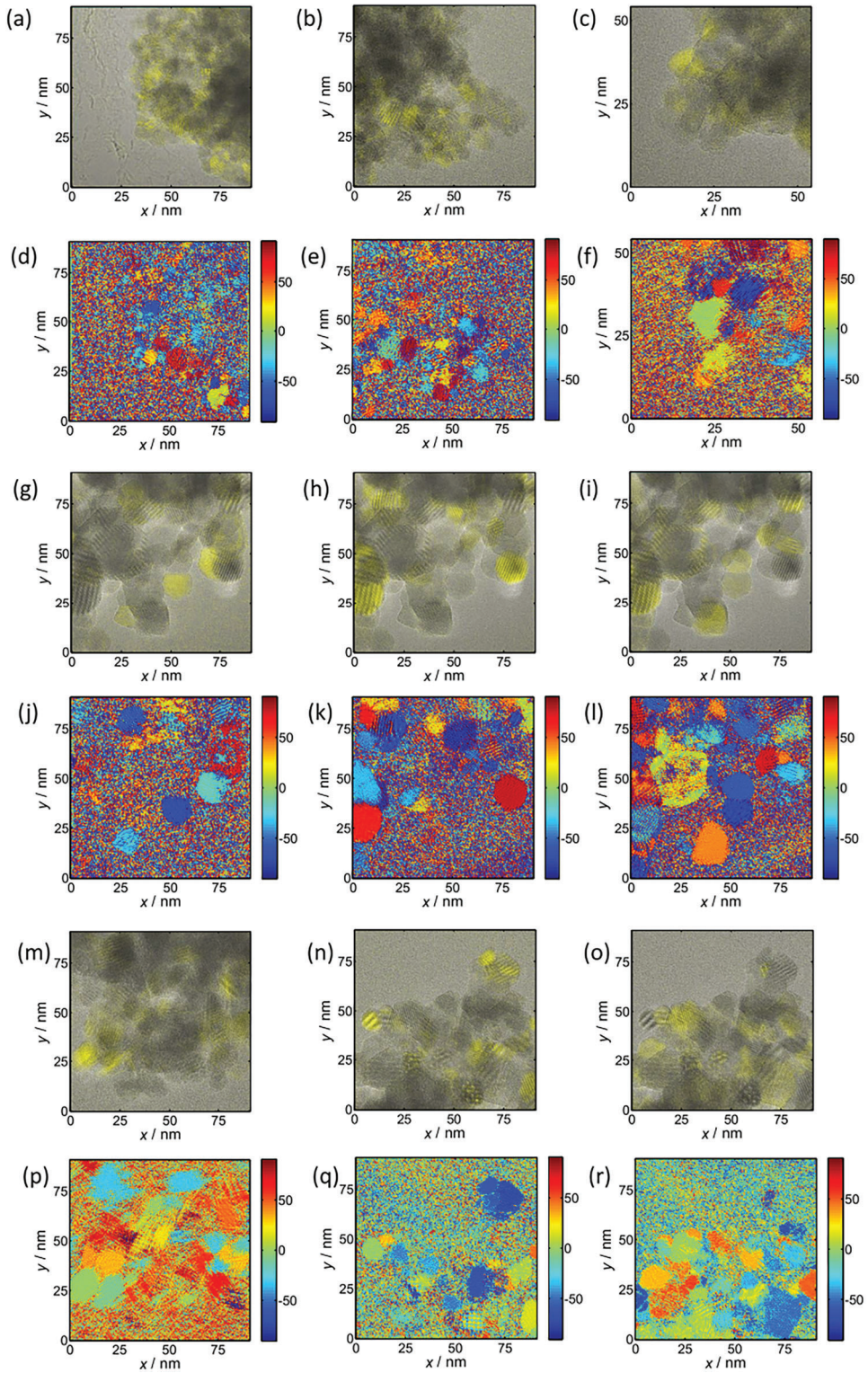

Figure 4. HRTEM images with intensity-colorized maps and corresponding rotation maps, where all crystallites with fringe periodicity corresponding to the analyzed lattice reciprocal vector are shown as colored patches with hue denoting the orientation of the crystal lattice in the image plane. All images portray NF tips. a–c) Colorized HRTEM images and d–f) corresponding rotation maps, where all crystallites with fringe periodicity corresponding to the [111] lattice reciprocal vector; the images refer to NFs a,d) NiZn-500, b,e) CoNi-500 and c,f) CoNi-600. g–i) Colorized HRTEM images and j–l) corresponding rotation maps for the reciprocal vectors [111], [220] and [222]/[311] of a CoZn-600 NF. m) Colorized HRTEM image m) and p) corresponding rotation maps for the [220] direction of a CoZn-500 NF. n,o) Colorized HRTEM images and q,r) corresponding rotation maps for the reciprocal vectors [220] and [222]/[311] of a NiZn-600 NF.

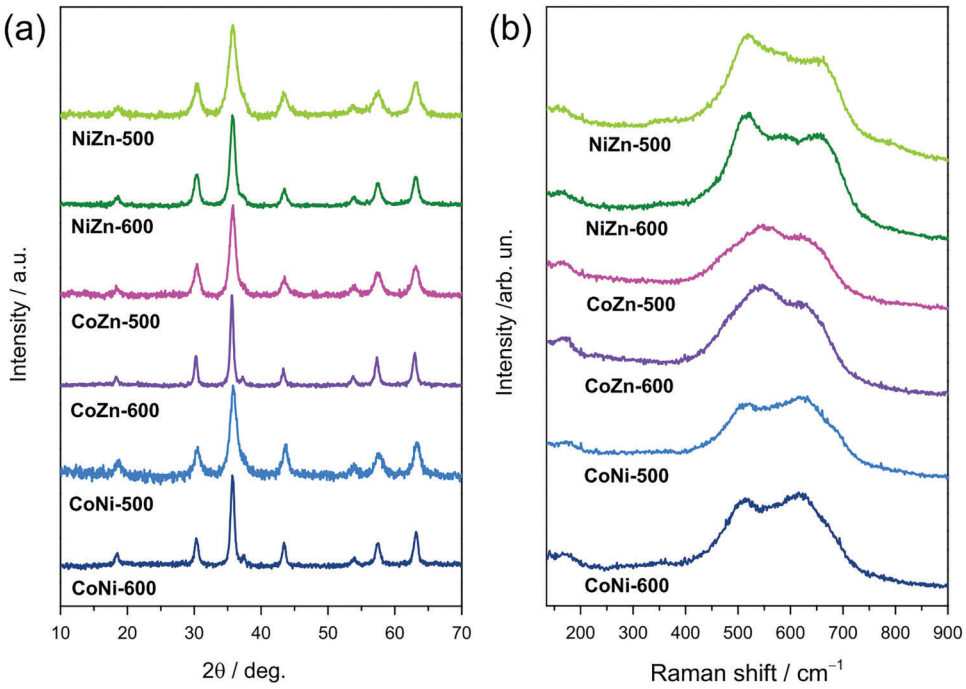

Figure 5. a) XRD patterns and b) averaged micro-Raman spectra of the samples.

As expected,[41,43] for a given oxide composition, larger values of the average size of the HESO crystallites pertain to the NFs calcined at higher temperature (bottom of Figure S6, Supporting Information). At given T_C, the crystallite size increases in the same order as that of nanograins (NiZn < CoNi <CoZn). The lattice parameter (a) is 8.294, 8.319 and 8.312 Å for CoNi-500, CoZn-500 and NiZn-500, respectively. As T_C is increased at 600 °C, a increases to 8.327, 8.349 and 8.322 Å, in line with literature reports for the temperature range here considered.[52,53]

Figure 5b displays the micro-Raman spectra obtained by averaging all spectra collected to evaluate the spatial homogeneity of each sample (see Figure S7, Supporting Information). Five Raman-active normal vibration modes (A_{1g} + E_g + $3F_{2g}$) are predicted for the spinel structure (*Fd-3m* space group).[54–58] Their frequency positions and relative intensities depend on the radii of cations in the oxide lattice[56] and strongly vary within the family of spinels.[55,56,59–62] An in-depth discussion on the phonon modes detected in electrospun high-entropy (Cr,Mn,Fe,Co,Ni), (Cr,Mn,Fe,Co,Zn) and (Cr,Mn,Fe,Ni,Zn) oxide NFs produced by calcination at 900 °C has been reported in a previous paper.[28] The spectra of $(Cr_{1/5}Mn_{1/5}Fe_{1/5}Co_{1/5}Ni_{1/5})_3O_4$, $(Cr_{1/5}Mn_{1/5}Fe_{1/5}Co_{1/5}Zn_{1/5})_3O_4$ and $(Cr_{1/5}Mn_{1/5}Fe_{1/5}Ni_{1/5}Zn_{1/5})_3O_4$ calcined at lower T_C do not significantly differ from them except for slight intensity changes. In the case of CoZn and NiZn NFs, the mode A_{1g}, involving the vibration along the direction joining an oxygen atom to a M^{2+} cation,[28] intensifies with increasing T_C, in agreement with the literature.[63] This spectral change can be ascribed to the cation redistribution.[63] Besides, for a given HESO composition, in the spectra of the fibers calcined at 500 °C the spectral features are less resolved than in those calcined at 600 °C (and 900 °C), as reasonably expected. This reflects the lower crystallinity degree of the oxide, the larger density of lattice defects and the smaller size of the crystallites/nanograins formed at lower T_C.[41,43] The fit of the spectra to Gaussian bands (Figure S8, Supporting Information) reveals that, besides the normal phonon modes, inversion-induced modes[44,56,64,65] also contribute to the Raman intensity in all samples, in full agreement with both previous studies[28] and other reports on HESO nanoparticles.[65]

XPS survey spectra (Figure S9, Supporting Information) reveal that the surface of the investigated materials is composed by (adventitious) carbon, oxygen, chromium, manganese and iron. In addition, cobalt and nickel are detected for CoNi NFs, cobalt and zinc for CoZn NFs, and nickel zinc for NiZn NFs. High-resolution XPS studies allow us to determine the oxidation state of each analyzed element and quantify their concentration. In particular, the total chemical composition of the surface of the investigated materials is summarized in Table S2 (Supporting Information). At lower T_C, the concentration of metal cations present in the NF surface layers is larger. In the 2p spectral region of TMs (**Figure 6**), a couple of peaks is always present (i.e., $2p_{3/2}$ and $2p_{1/2}$), due to the spin-orbit splitting phenomenon. In the $2p_{3/2}$ region (see Figure 6a) it is observed the presence of three different features, which are attributed to: i) chromium is present as Cr(III) oxide, peaking at ≈575.8 eV; ii) Cr(III) hydroxide, centered at ≈576.9 eV; and iii) Cr(VI) oxide, peaking at ≈578.9 eV.[66–68] It is interesting to observe that the metal composition and T_C, have a strong influence on the abundance of Cr(VI) species. In particular, at T_C = 500 °C the Cr(VI) relative abundance raises in the order CoZn < CoNi < NiZn, reaching values of 7.17, 18.83 and 21.62%at., respectively. Moreover, these values decrease when T_C is increased: i) from 7.17 to 6.52%at. for CoZn; ii) from 18.83 to 12.61%at. for CoNi; and iii) from 21.62 to 1.62%at. for NiZn. Only one peak centered at ≈1021.4 eV is observed in the Zn $2p_{3/2}$

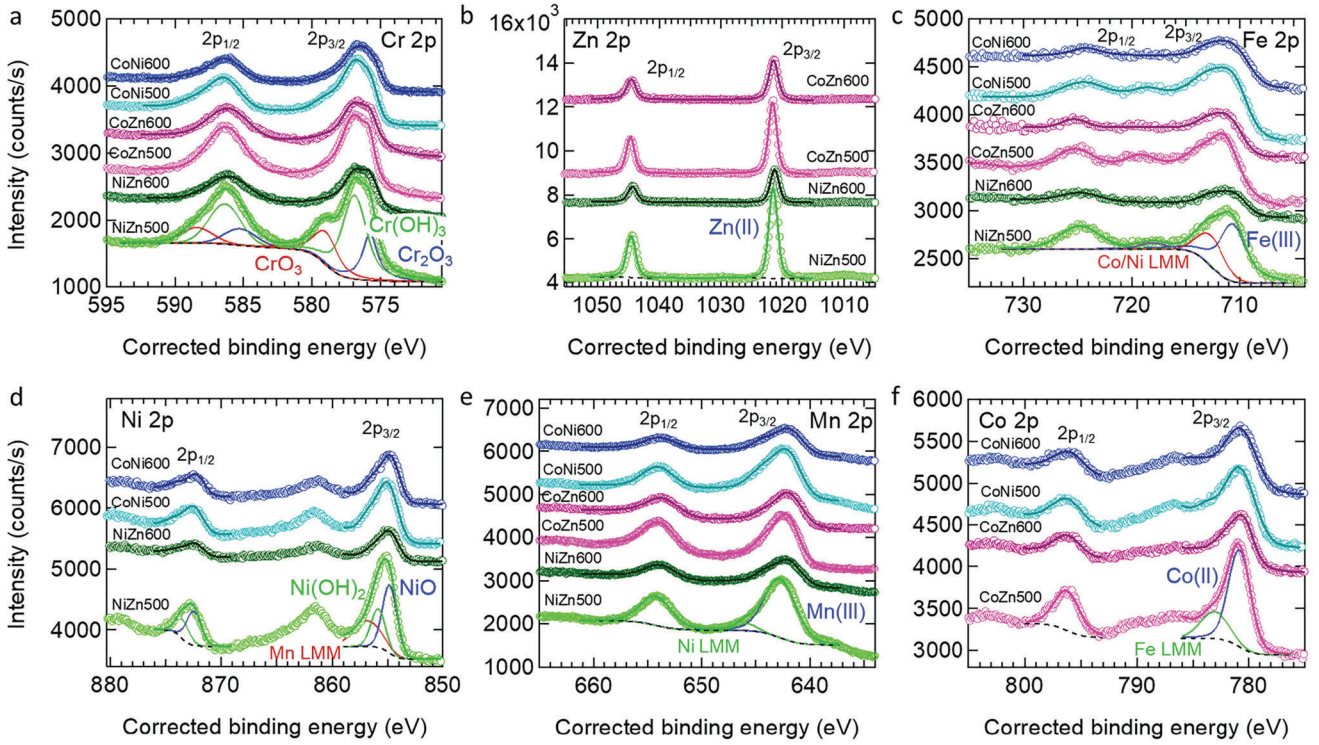

Figure 6. Results of the high resolution XPS studies and fitting analysis in the different spectral regions: a) Cr 2p, b) Zn 2p, c) Fe 2p, d) Ni 2p, e) Mn 2p and f) Co 2p core levels.

region (see Figure 6b), which is attributed to Zn(II) species.[69] Analyzing the Fe2p$_{3/2}$ spectral region, there is not a clear evidence that iron is present in more than one oxidation state (Figure 6c).

Indeed, iron is probably present as Fe(III), since the 2p$_{3/2}$ transition is present at ≈710.7 eV.[69] On the other hand, two different features are detected (Figure 6d), which are attributed to the presence of: i) NiO species, with the peak centered at ≈854.8 eV [70] and ii) Ni(OH)$_2$ species, peaking at ≈856.3 eV.[71] The absence of satellite peaks in the Mn2p$_{3/2}$ spectral region (Figure 6e) allows to confirm the absence of Mn(II) species. Moreover, the broadening of the peak and its position centered at ≈642.0 eV indicate that manganese is present *mainly* as Mn(III).[24] Finally, cobalt is present only as Co(II) species (Figure 6f), with the peak centered at ≈780.6 eV.[72] In some of the analyzed spectral regions, Auger lines of several TMs are detected, which are assigned directly in Figure 6. The total chemical composition of the surface of the investigated materials is summarized in Table S2 (Supporting Information). At lower T_C, the concentration of metal cations present in the NF surface layers is larger. On the other hand, a higher concentration of oxygen species is detected at greater T_C. In CoNi samples, the surface atomic concentration of Ni, Cr and Mn is similar to the nominal value. A higher Co surface content is observed for both the CoNi materials at the expenses of Fe. For CoZn, the surface is richer in Cr, Mn and Zn and poorer in Co and Fe with respect to the bulk. Finally, in NiZn the Ni and Fe surface concentration is lower than the nominal value, that of Cr and Zn higher, and for Mn it is exactly the same. It is interesting to observe that these conclusions are independent from T_C, indicating that the calcination temperature has a minor role in the modulation of the distribution of metals between the surface and the bulk. On the other hand, as T_C raises it is observed a migration of Co and Fe from the surface to the bulk of the HESO-electrocatalysts, while Ni, Cr and Mn show the opposite trend. No differences in Zn surface composition are observed between the samples calcinated at different temperatures.

The oxygen 1s transition of all the samples is composed by four features (**Figure 7**): i) at ≈530.1 eV, lattice oxygen atoms (O_L) are detected;[66,73–75] ii) the peak at ≈531.3 eV, commonly attributed to "oxygen vacancies"(O_V),[75–77] comes from oxygen atoms in the neighborhood of lattice oxygen vacancies, which according to a recent computational paper[78] are surface −OH groups saturating O vacancies,[79] and iii) at higher binding energies (i.e., 532.3 and 533.6 eV), features are attributed to the adsorbed or chemisorbed oxygen species such as O_2 or H_2O.[23,28,77] Quantitative results of the different oxygen species are summarized in Table S3 (Supporting Information). It is revealed that samples calcined at 600 °C have a lower concentration of O_L species with respect to those calcined at 500 °C. The highest concentration of surface O_Vs is detected for CoZn samples, while NiZn samples exhibit the lowest O_V concentration. On T_C, a 2- to 3-fold increase in the amount of adsorbed or chemisorbed oxygen species is detected for all the samples. This indicates that the calcination temperature has a pivotal role in the modulation of the oxophilicity/oxophobicity of the surface of the HESO-electrocatalysts.

In normal spinels, $[M^{2+}]_{8a}[M^{3+}{}_2]_{16d}O_4$, divalent and trivalent cations occupy 8*a* (tetrahedral) and 16*d* (octahedral) sites, respectively.[49,80,81] Conversely, in (partially) inverse spinels, $[M^{2+}{}_{1-\xi}M^{3+}{}_{\xi}]_{8a}[M^{2+}{}_{\xi}M^{3+}{}_{2-\xi}]_{16d}O_4$, a fraction of trivalent cations

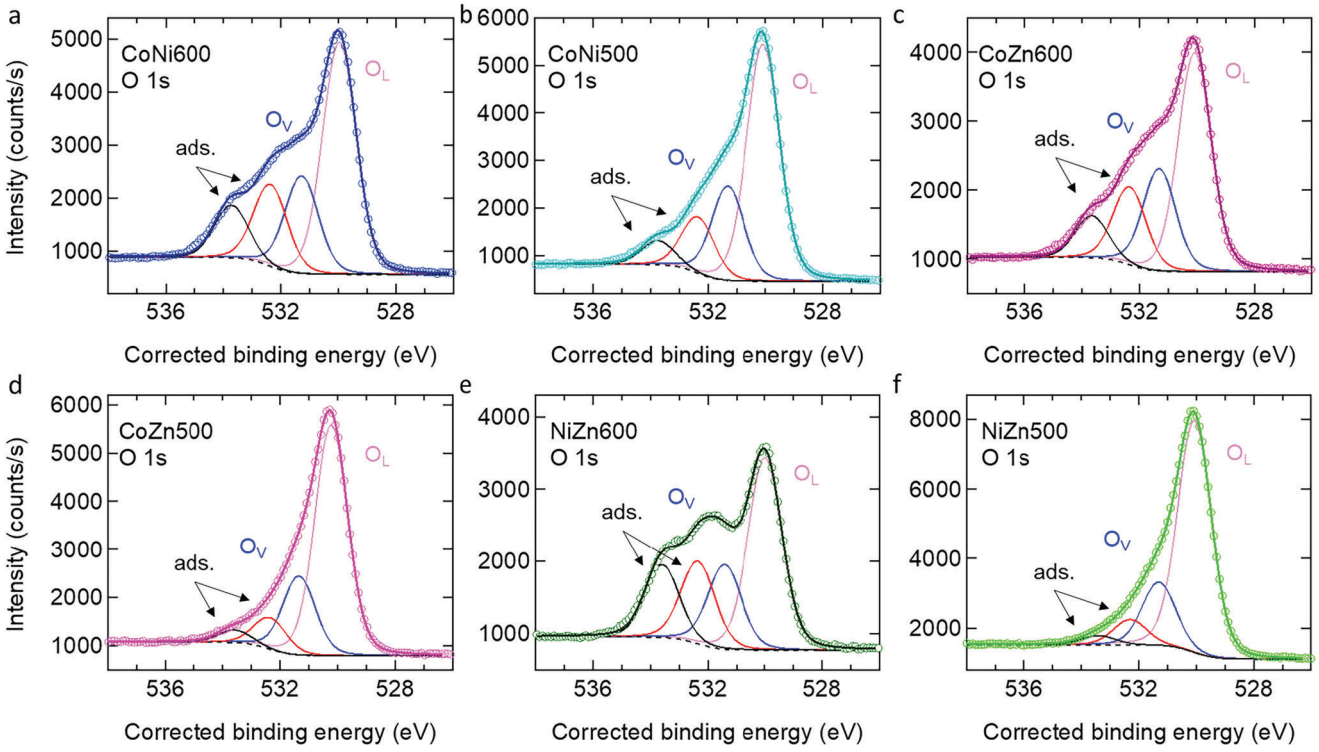

Figure 7. Results of the high resolution XPS studies and fitting analysis in the O 1s spectral region of the six different samples: a) CoNi-600, b) CoNi-500, c) CoZn-600, d) CoZn-500, e) NiZn-600 and f) NiZn-500.

($0 < \xi < 1$) replace the divalent ones at tetrahedral sites. If the inversion degree $\xi = 1$, spinels have inverse structure, $[M^{3+}]_{8a}[M^{2+}M^{3+}]_{16d}O_4$.[49,80,81] The inversion degree heavily affects the physicochemical properties of spinels. It is strongly influenced by the MC,[26,28,56,59,80] and T_C.[25,81,82] At lower T_C, due to kinetic effects (thermodynamic equilibrium is not yet reached), trivalent cations with a high octahedral site preference energy occupy *also* the tetrahedral sites.[41,42] For a given T_C, the inversion degree of the HESOs investigated, as *qualitatively* monitored by the A_{1g}'/A_{1g} band intensity ratio (Figure S8, Supporting Information), varies in the order CoNi > NiZn > CoZn, as previously reported for HESO NFs calcined at higher T_C.[28] In CoZn and NiZn NFs, the A_{1g}'/A_{1g} band intensity ratio decreases with increasing T_C, signaling the decrease of ξ; oppositely, in CoNi NFs, it slightly increases.

According to the cation distributions previously proposed for HESO NFs calcined at 900 °C,[28] based on simple consideration of electronegativity and crystal-field octahedral stabilization energy, at thermal equilibrium Cr^{3+} and Mn^{3+} occupy *only* 16*d* sites, as most frequently reported,[41,83] Zn^{2+} resides on 8*a* sites, while the remaining cations (Fe^{3+}, Co^{2+} and Ni^{2+}, based on the results of the XPS analysis) may accommodate both in octahedral and tetrahedral sites. In particular, in (Cr,Mn,Fe,Co,Zn) and (Cr,Mn,Fe,Ni,Zn) HESO NFs, 2/3 of Fe^{3+} cations accommodate in tetrahedral sites ($\xi = 0.4$), while in (Cr,Mn,Fe,Co,Ni) HESO NFs, all Fe^{3+} cations and 1/3 of Co^{3+} occupy 8*a* sites ($\xi = 0.8$).[28] Sarkar et al.[83] using X-ray, Mössbauer, and neutron techniques proposed an analogue cation distribution, with 1/3 of Ni^{3+} (in place of Co^{3+}) in tetrahedral sites, for micrometer-sized $(Cr_{1/5}Mn_{1/5}Fe_{1/5}Co_{1/5}Ni_{1/5})_3O_4$ HESO. At lower T_C, the cation distribution can be reasonably assumed to be intermediate between a completely random distribution (CRCD) and the equilibrium distribution (ECD) of cations just described. In the latter, cations are randomly distributed within each 16*d* and 8*a* sublattice, but the cation partition between the two sublattices is dictated by the different cation energetic preference for 16*d* sites, as in the case of HESO NFs calcined at 900 °C (ECD).[28] A completely random cation distribution amounts to a situation where each cation is present in the 8*a* and 16*d* sublattice with 1:2 ratio. Thus, the cation distribution in NFs calcined at low temperature is expected to be between the two above distributions: the closer to the fully random situation, the lower the calcination temperature (**Figure 8**). For the CRCD, the inversion degree is $\xi = 2/3 \cong 0.67$ for all MCs, whereas for the ECD, ξ has the value 0.80, 0.40, and 0.40 for CoNi, CoZn, and NiZn NFs, respectively.[28] Therefore, *incomplete* attainment of the ECD corresponds to a *lower* inversion degree for CoNi, and to a *higher* one for CoZn and NiZn. Regarding the catalytically important occupation of 16*d* sites by highly active Co^{2+}/Co^{3+} cations, incomplete attainment of the ECD corresponds to higher occupation for CoNi (Figure 8a) and to a lower one for CoZn NFs (Figure 8b). Moreover, it promotes the occupation of octahedral sites by electrocatalytically inert Zn^{2+} cations in both CoZn and NiZn NFs (Figure 8b,c).

Despite its extreme simplicity and the underlying drastic approximations, the scheme proposed here to depict the changes induced by the lower T_C in the cation distributions is capable to *qualitatively* account for the variation of the inversion degree, as resulting from the MRS analysis. Besides, it provides useful

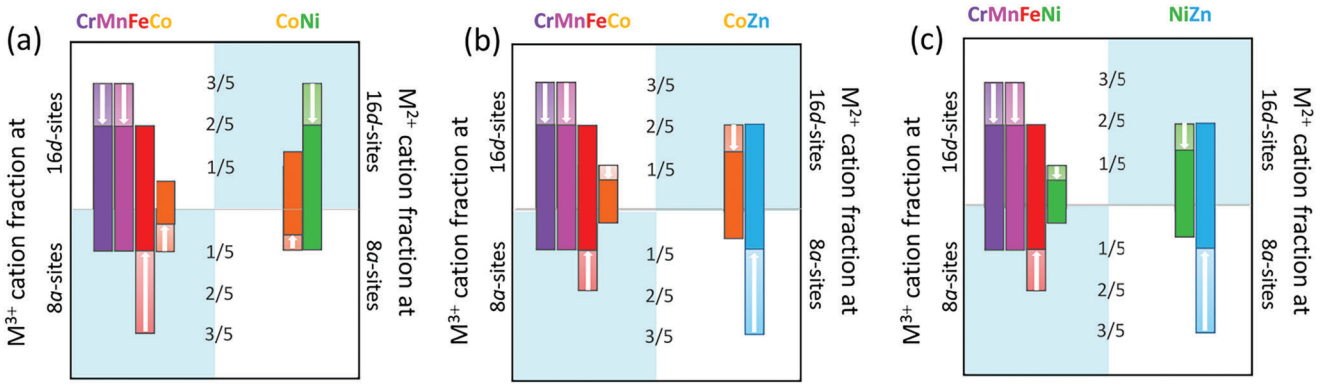

Figure 8. Changes in the cation distributions for the a) CoNi, b) CoZn and c) NiZn NFs promoted by the T_C lowering. Dark colors indicate the CRCD, light colors the ECD. The cation distribution in NFs calcined at low temperature is expected to be between these two distributions. The total molar fraction of each cation is 3/5, including both oxidation states (2+ or 3+) and types of sites (tetrahedral or octahedral).

indications for the understanding of the electrochemical behavior of HESO-based OER electrocatalysts (see below).

2.2. Electrocatalytic Performance

The OER performance of the HESO-based electrocatalysts was tested at room temperature (RT) in 1 M KOH electrolyte solution using a three-electrode setup. Their structural stability was investigated by carrying out ex situ MRS analysis on the fresh and reacted electrodes (see Supporting Information). Their structural stability was investigated by carrying out ex situ MRS (Figure S11, Supporting Information), TEM, EDX and electron diffraction analyses (Figure S12, Supporting Information) on the fresh and reacted electrodes. The comparison of the recorded spectra indicates that the catalysts are fairly stable (see Supporting Information). In order to evaluate the catalytic activities of CoNi, CoZn and NiZn NFs toward the OER and the reaction kinetics, the polarization curves (**Figure 9**a; Figure S13, Supporting Information) were recorded in linear sweep voltammetry (LSV) mode and the slopes of the Tafel curves (Figure 9b) were calculated. The results obtained, shown in Figure 9c,d, indicate that their performance depends on both the MC and T_C. As a general trend, the lower the overpotential (η_{OER}), the better the catalytic activity since a lower overvoltage is required to obtain the same current density;[84,85] since Tafel slope (β_{OER}) refers to the acceleration of electron transfer and electron migration during the catalytic process, the lower its value, the faster the reaction kinetics, i.e., the higher the current density at a given potential.[84]

The values of β_{OER} and η_{OER} obtained in the present study well compare with those reported in the literature for other high-entropy oxides and the common benchmark catalysts (Table S4, Supporting Information). At 10 mA cm^{-2}, regardless of T_C, η_{OER} decreases in the order CoZn > NiZn > CoNi (Figure 9c). At higher current density (20 mA cm^{-2}), higher values of η_{OER} are obtained, varying in the same order (Figure S14, Supporting Information). Thus, the same ranking of electrocatalytical activity in the OER occurs as previously observed in the HEO NFs calcined at higher temperature:[23] CoZn < NiZn < CoNi (Figure S15a, Supporting Information). β_{OER} decreases in the order NiZn > CoZn > CoNi (Figure 9d) pointing at an improvement of the OER kinetics in the opposite order (i.e., NiZn < CoZn < CoNi). Interestingly, the electrochemical performance of CoNi NFs is better at T_C = 500 °C than at T_C = 600 °C, whereas the opposite occurs for that of CoZn and NiZn NFs.

According to the adsorbate evolution mechanism (AEM),[21,26,34,86–88] in an alkaline solution, the OER progresses through the following four steps (**Figure 10**a) each of which involves the release of one electron (e^-): 1) adsorption of OH^- at the catalyst surface (denoted as *) and formation of the adsorbed *OH species, $* + OH^- \rightarrow *OH + e^-$; 2) reaction of *OH with OH^- and formation of the adsorbed *O species, accompanied by release of a water molecule, $*OH + OH^- \rightarrow *O + H_2O + e^-$; 3) reaction of *O with OH^- and formation of the adsorbed *OOH species, $*O + OH^- \rightarrow *OOH + e^-$; 4) reaction of OH^- with *OOH and formation of $*O_2$, which leaves the catalyst surface in the gas form (O_2) together with a water molecule, $*OOH + OH^- \rightarrow *O_2 + H_2O + e^-$.

2.2.1. Dependence of η_{OER} and β_{OER} on the Number of outer 3D-Electrons

It is widely recognized that the OER catalytic activity is determined to a large extent by the adsorption energies of reaction intermediates. The latter weakens systematically with increasing number of outer electrons.[89] According to the *d*-band model, high/low reactivity (strong/weak binding) pertain to early/late TMs.[89] The number of outer 3*d*-electrons (referred to the M_3O_4 formula unit, FU), as calculated from the cation distributions satisfying electroneutrality (Figure 8), is 16.0, 17.2, and 17.8 for $(Cr_{1/5}Mn_{1/5}Fe_{1/5}Co_{1/5}Ni_{1/5})_3O_4$, $(Cr_{1/5}Mn_{1/5}Fe_{1/5}Co_{1/5}Zn_{1/5})_3O_4$ and $(Cr_{1/5}Mn_{1/5}Fe_{1/5}Ni_{1/5}Zn_{1/5})_3O_4$, respectively. Therefore, the three equimolar MCs *effectively* behave as metals M with outer 3*d*-electron numbers 5.3, 5.7 and 5.9, respectively. In other words, although the Zn^{2+} cation ($3d^{10}$) is unlikely to take part in the OER, including its outer electrons in the calculation allows to take into account its inactivity/low activity, as a greater number of outer 3*d*-electrons reflects in a weaker binding with reaction intermediates and, thus, in a worse electrocatalytic performance.[89] Indeed, by plotting η_{OER} as a function of the outer 3*d*-electron number per M_3O_4 FU (N_{3d}, Figure 10b),

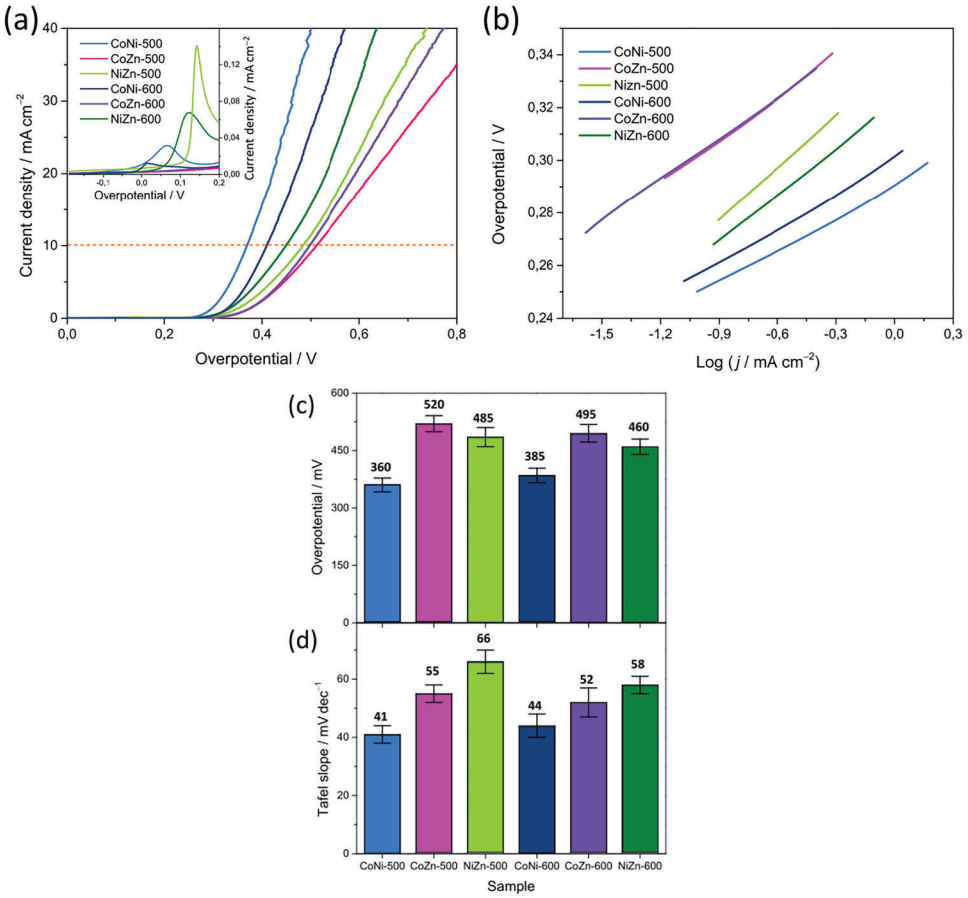

Figure 9. Results of the electrochemical measurements. a) LSV curves recorded at a scan rate of 5 mV s^{-1} in 1.0 M KOH (pH≈13.8) for different HESO samples as electrocatalysts and b) corresponding Tafel curves. c) OER overpotentials and d) Tafel slopes measured at 10 mA cm^{-2}.

regardless of T_C – 500, 600 °C (present work) or 900°C (previous work[23]) – a non-monotonic trend is obtained. This suggests that for overpotential also other factors are influential (e.g., morphology, since CoZn NFs differ from the remaining ones for the larger average size of the oxide grains/crystallites). On the contrary, β_{OER} generally increases monotonically with N_{3d} (Figure 10c): the higher the outer 3*d*-electron number, the more sluggish the reaction kinetics. Therefore, this composition-dependent descriptor accounts well for most of the variation of β_{OER}.

2.2.2. Dependence of β_{OER} on the Occupation of e_g Orbitals at the Octahedral Sites

Also the *occupation of* e_g *orbitals* at the octahedral sites is believed to affect the binding strength of OER reaction intermediates.[42] The optimal OER activity is expected at a moderate e_g filling ($e_g \approx 1$), which balances the competition between rate-limiting steps.[42] At high T_C (ECD), the e_g filling, referred to the M_3O_4 FU, is 2.2 for all MCs. At low T_C (CRCD), the e_g filling is 2.8, 3.6 and 3.6 for $(Cr_{1/5}Mn_{1/5}Fe_{1/5}Co_{1/5}Ni_{1/5})_3O_4$, $(Cr_{1/5}Mn_{1/5}Fe_{1/5}Co_{1/5}Zn_{1/5})_3O_4$ and $(Cr_{1/5}Mn_{1/5}Fe_{1/5}Ni_{1/5}Zn_{1/5})_3O_4$, respectively. Since the optimal e_g filling (e_g^*) referred to the M_3O_4 FU is 3, in the case of CoNi NFs, increasing T_C causes the e_g filling to progressively deviate from e_g^* value, which explains the monotonic worsening (β_{OER} increase) observed moving from CoNi-500 to CoNi-900 (Figure 10c; Figure S15b, Supporting Information). Instead, in the case of NFs containing Zn, the increase of T_C first causes the e_g filling to decrease and approach e_g^* (with consequent improvement); while a further increase in T_C, on the contrary, causes the e_g filling to move away from its optimal value (which induces a worsening). This descriptor explains the composition-dependent monotonic versus non-monotonic variation of β_{OER} with T_C (see also Figure S15b, Supporting Information).

2.2.3. Dependence of η_{OER} on the Occupation of Octahedral Sites

The changes in the occupation of octahedral sites induced by the variation of T_C represent another aspect related to the cation distribution that also has a great influence on the electrocatalytic behavior of the HESO fibers. In the case of CoNi NFs, incomplete attainment of the ECD (Figure 8a) corresponds to higher occupation of 16*d* sites by highly active[24,27,32,86,90] Co^{2+} and Co^{3+} cations. The same consideration would apply to Ni^{2+} and Ni^{3+} cations if the distribution of cations proposed by Sarkar et al.[83]

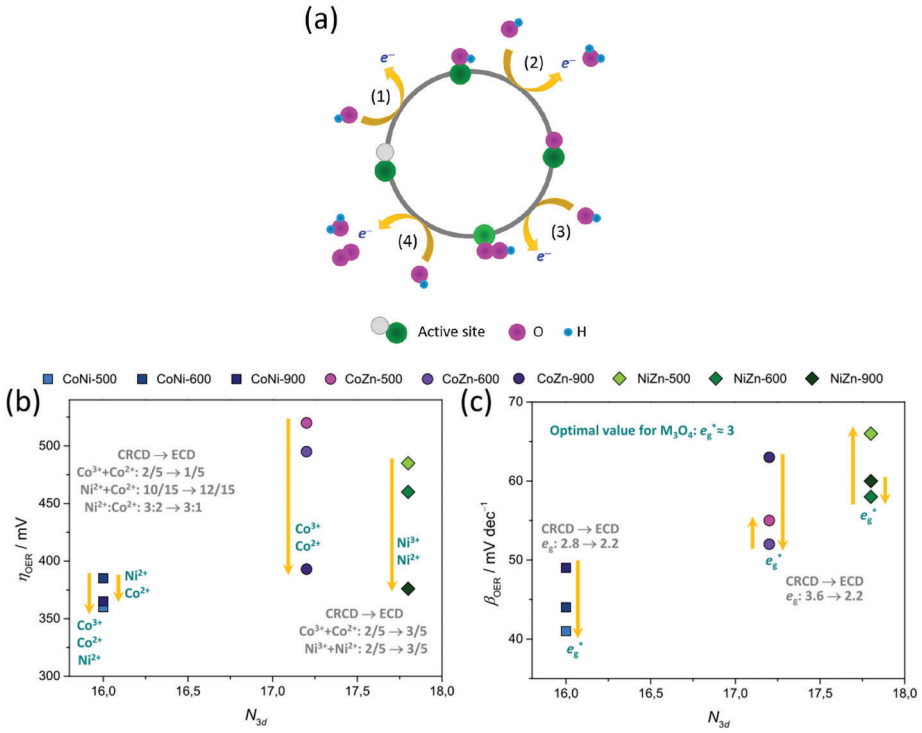

Figure 10. a) Reaction mechanism for the OER in the alkaline environment, with oxygen deficient coordinately unsaturated metal octahedra MO_{6-x} on the surface acting as the active centers for the OER (lighter green sphere indicates a metal cation with 3+ oxidation state). b) OER overpotentials (η_{OER}) and c) Tafel slopes (β_{OER}) at 10 mA cm^{-2} as a function of the outer 3D-electron number for M_3O_4 FU (N_{3d}). The data relative to the electrospun (Cr,Mn,Fe,Co,Ni), (Cr,Mn,Fe,Co,Zn) and (Cr,Mn,Fe,Ni,Zn) HESO NFs calcined at 900 °C[23] are also reported.

was assumed to be the equilibrium distribution. Actually, a peak, attributable to the oxidation of Co^{2+}/Co^{3+} (Ni^{2+}/Ni^{3+}) cations to Co^{3+}/Co^{4+} (Ni^{3+}/Ni^{4+}) cations after activation,[65,86] is detected in the LSV curves of CoNi NFs in the low-voltage region (inset of Figure 9a and Supporting Information), which hints at catalyst surface restructuring with formation of cobalt (nickel) oxyhydroxide, CoOOH (NiOOH),[35] responsible for the redox sites acting as OH^- adsorption sites.[86] The results of ex situ Raman scattering and HRTEM/EDX measurements on the used catalysts prove the formation of nanoplatelets of oxyhydroxide on the fiber surface (see Supporting Information). The lower the temperature of the thermal treatment, the higher the intensity of this peak in the investigated NFs. Instead, the increased octahedral occupation by Co^{2+} and Ni^{2+} cations (and/or the increased Ni^{2+}:Co^{2+} ratio) might be responsible for the η_{OER} lowering observed moving from CoNi-600 to CoNi-900. In the case of Zn-containing HESOs, the decrease of T_C favors the occupation of 16*d* sites by Zn^{2+} cations at expense of the occupation by the most redox-active[24,32,86,90] Co^{2+}/Co^{3+} and Ni^{2+}/Ni^{3+} species in CoZn and NiZn NFs, respectively (Figure 8b,c). This reflects in the progressive worsening in the catalytic activity (η_{OER} increase) observed in CoZn and NiZn NFs with increasing T_C (Figure 10b).

2.2.4. Dependence of β_{OER} on the OV Concentration

As mentioned above, defect engineering has recently emerged as a viable strategy to improve the electrocatalytic performance of nanomaterials.[21,30–35] Among the various type of defects, point defects and in particular vacancy defects are the most exploited in OER.[21] Cationic vacancies require higher formation energy compared to anionic vacancies.[10] Among anionic vacancies, OVs with low formation energy are most frequently used to enhance OER performance.[21,30–35,91] Thus, it is not surprising that an increase in their surface concentration (x_{OV}) as revealed by XPS data, results in lower charge transfer resistance (Figure S15b, Supporting Information) and faster kinetics (Figure S14, Supporting Information), in agreement with previous studies.[23]

As for the OER kinetics, it is worthwhile noticing that the variation of x_{OV}, alone, cannot explain all changes in β_{OER}. OVs provide adsorption sites for the reaction intermediates,[78,79] but the results in terms of kinetics obviously depends also on the reactivity of the metal cation in the O-deficient coordinatively unsaturated octahedron MO_{6-x} acting as the active centers for the OER.[27] Thus, comparable OV concentrations (as in the case of CoNi-500 and CoZn-600) result in different β_{OER} values (Figure S17, Supporting Information). Since the adsorption energies of reaction intermediates decreases with increasing N_{3d},[89] we propose that the dependence of β_{OER} on x_{OV} and N_{3d} can be modeled by the power law x_{OV}^{α}, where the exponent $\alpha = {N_{3d}}^0/N_{3d}$, with ${N_{3d}}^0$ the number of 3*d* electrons of the most active (Cr,Mn,Fe,Co,Ni) combination, accounts for the metal (combination)-dependent reactivity.

Despite the extreme simplicity of this model, which neglects the effects of the variation of cation-distribution, morphology and

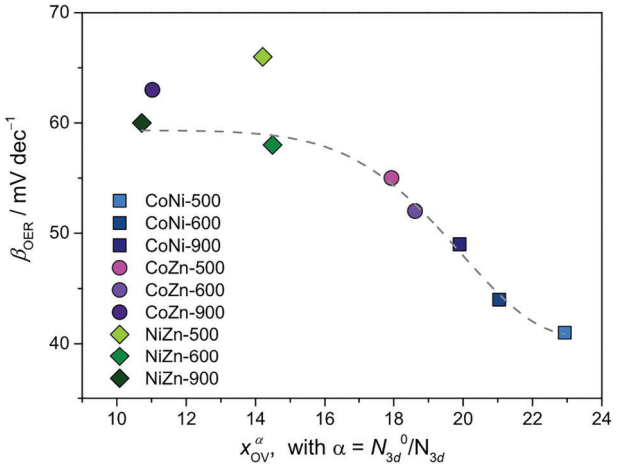

Figure 11. Plot of β_{OER} as a function of $x_{OV}{}^{\alpha}$, where x_{OV} is the OV concentration and the exponent $\alpha = N_{3d}{}^{0}/N_{3d} = 1.00$, 0.93 and 0.90, for CoNi, CoZn and NiZn NFs, respectively. The data relative to the HESO NFs calcined at 900 °C[23] are also reported.

crystallinity, the representative points of most NF catalysts line up along a single β_{OER} ($x_{OV}{}^{\alpha}$) curve (**Figure 11**). Thus, the decrease of β_{OER} (faster kinetics) is *mainly* due to the increase in x_{OV} (number of adsorption sites), as amplified by the decrease in N_{3d} toward its optimal value $N_{3d}{}^{0}$ (increase in reactivity). Exceptions are the CoZn-900 and NiZn-500 catalysts, which have e_g filling far from its optimal value (Section 2.2.2, Figure 10c) and seem less effective in facilitating the formation of the surface oxido species *O than the other catalysts, to the extent that the formation of *O is the rate-determining step, whereas in the OER catalyzed by the other NFs the rate-determining step is the formation of *OOH and $*O_2$ species (see Supporting Information).

2.2.5. Long-Term Stability of the Best Performing Electrocatalyst

To evaluate the long-term stability of the best performing electrocatalyst (CoNi-500), chronopotentiometric measurements were carried out in 1 M KOH at a current density of 40 mA cm^{-2} for a duration of 3 h (Figure S18a, Supporting Information) and of 100 mA cm^{-2} for a duration of 1.5 h (Figure S18b, Supporting Information). The results demonstrate that the catalyst is satisfactorily stable: only slight variations in the overpotential are observed after continuous operation at the two current densities (≈38 mV at 40 mA cm^{-2} for 3 h, and ≈140 mV at 100 mA cm^{-2} for 1.5 h). In addition, as shown in the insets of Figure S18 (Supporting Information), the LSV polarization curves do not undergo significant changes after the application of a current density of 40 and 100 mA cm^{-2}. In the former case, the shift in overpotential is 19, 28 and 29 mV at current densities of 10, 30 and 50 mA cm^{-2}, respectively; in the latter case, the shift in overpotential is 43, 91 and 131 mV at current densities of 10, 50 and 100 mA cm^{-2}, respectively.

The calculation[23] of the turnover frequency (TOF) leads to a value of $2.81 \cdot 10^{-2}$ s^{-1} that exceeds that reported for nanoporous $(Cr_{0.2}Mn_{0.2}Fe_{0.2}Co_{0.2}Ni_{0.2})_3O_4$ prepared by solution combustion at low temperature ($6.64 \cdot 10^{-3}$ s^{-1}).[32] Outstandingly, the production rate of CoNi-500 is 368.9 mmol O_2 h^{-1} g^{-1} with a Faradaic efficiency (FE) of 95.40%, higher than that reported for nanoporous $(Cr_{0.2}Mn_{0.2}Fe_{0.2}Co_{0.2}Ni_{0.2})_3O_4$ (85.21%).[32] The specific production rate of O_2 largely exceeds that of Ni_3N nanoparticles supported on a benzimidazole covalent organic framework (230 mmol O_2 h^{-1} g^{-1}),[92] one of the highest reported in the latest years.

3. Conclusion

High-entropy spinel (Cr,Mn,Fe,Co,Ni), (Cr,Mn,Fe,Co,Zn) and (Cr,Mn,Fe,Ni,Zn) oxide nanofibers, having granular architecture and oxygen-deficient surface, are produced by electrospinning and calcination at low temperature (600 or 500 °C) and are evaluated as electrocatalysts for OER in alkaline medium. The study of their physicochemical properties by means of SEM, TEM, XRD, XPS and Raman spectroscopy allows concluding that the variation of their composition and calcination temperature T_C produces complex and interdependent changes that reflect in different electrocatalytic performance, as determined by both the density of the so-called oxygen-vacancies and by reactivity-related descriptors, such as the number of outer 3d electrons, occupation of e_g orbitals at the octahedral sites, and occupation of octahedral sites by the most redox-active cationic species, which depend on composition and inversion degree of the spinel, and cation distribution in the lattice.

The outer 3d-electron number referred to the M_3O_4 formula unit increases in the order $(Cr_{1/5}Mn_{1/5}Fe_{1/5}Co_{1/5}Ni_{1/5})_3O_4$ (16.0) < $(Cr_{1/5}Mn_{1/5}Fe_{1/5}Co_{1/5}Zn_{1/5})_3O_4$ (17.2) < $(Cr_{1/5}Mn_{1/5}Fe_{1/5}Ni_{1/5}Zn_{1/5})_3O_4$ (17.8). The variation of T_C affects not only the morphology and crystallinity of the fibers and the concentration of the oxygen-vacancies on their surface, but also the cation distribution in the oxide lattice and, hence, the e_g filling and the inversion degree ξ of the spinel. ξ increases with T_C for the (Cr,Mn,Fe,Co,Ni) combination, while decreases for the (Cr,Mn,Fe,Co,Zn) and (Cr,Mn,Fe,Ni,Zn) combinations. Lowering T_C promotes the occupation of octahedral sites by highly active Co^{2+}/Co^{3+} species in $(Cr_{1/5}Mn_{1/5}Fe_{1/5}Co_{1/5}Ni_{1/5})_3O_4$, while enhances the occupation by electrocatalytically inert Zn^{2+} cations in both $(Cr_{1/5}Mn_{1/5}Fe_{1/5}Co_{1/5}Zn_{1/5})_3O_4$ and $(Cr_{1/5}Mn_{1/5}Fe_{1/5}Ni_{1/5}Zn_{1/5})_3O_4$. Correspondingly, the occupation of e_g orbitals at the octahedral sites moves toward or away from its optimal value. The OER kinetics of the investigated fibers is mainly controlled by the simultaneous variation of the outer 3d-electron number and the surface oxygen-vacancy concentration.

$(Cr_{1/5}Mn_{1/5}Fe_{1/5}Co_{1/5}Ni_{1/5})_3O_4$ nanofibers calcined at 500°C exhibit the lowest overpotential and Tafel slope (360 mV and 41 mV dec^{-1}, respectively, at 10 mA cm^{-2}). Besides, they are able to operate continuously for 3 h at a current density of 40 mA cm^{-2} with only a small change in the overpotential (≈38 mV). Their outstanding production rate is 368.9 mmol O_2 h^{-1} g^{-1} with a FE of 95.40%.

The paper demonstrates that an accurate analysis of the results of the characterization of the pristine material by means of a combination of benchtop analytical techniques can provide relevant information for understanding its catalytic behavior.

The reported results constitute a solid basis for the rational optimization of the preparation conditions of high-entropy

spinel-oxide catalysts for OER, although no single recipe can be formulated to do that.

4. Experimental Section

Synthesis of the Electrospun HESO-Electrocatalysts: HESO-electrocatalysts were produced by electrospinning followed by calcination, as described in detail in a previous work.[28] The precursor solutions, based on equimolar combinations of (Cr,Mn,Fe,Co,Ni), (Cr,Mn,Fe,Co,Zn) and (Cr,Mn,Fe,Ni,Zn) were prepared via sol-chemistry. Electrospinning was operated via a CH-01 Electro-spinner 2.0 (Linari Engineering s.r.l.). Calcination was carried out in a muffle furnace at 500 or 600 °C for 2 h, increasing temperature at 10 °C min^{-1}. Further details are given in the Supporting Information.

Physicochemical Characterization: The morphology, texture, microstructure, crystalline phase and surface composition of the HESO-electrocatalysts were investigated by SEM, TEM, XRD, MRS and XPS. A Phenom Pro-X scanning electron microscope was utilized to acquire the SEM images, whereas HRTEM, HAADF-STEM and SAED analyses were carried out on a FEI Talos F200S scanning/transmission electron microscope, operated at 200 kV. Both microscopes were equipped with an EDX spectrometer for elemental mapping.

In order to get more detailed information on the NF inner morphology, projection analysis of STEM-EDX maps was carried out. Projection analysis consists in selecting a straight, constant-diameter NF (or region of a NF) and integrate (project) the map intensity along the NF axis. Then, the resulting transverse projection is fitted to models appropriate for solid or hollow NFs, namely:

$$I_{solid} = I_{background} + I_0 \sqrt{1-(r/R)^2} \quad (1)$$

$$I_{hollow} = I_{background} + I_0 \left(\sqrt{1-(r/R_{out})^2} - \sqrt{1-(r/R_{in})^2} \right) \quad (2)$$

where $I_{background}$ is the projected background intensity, I_0 is a constant depending on the NF size and composition, r is the distance from the NF axis, R is the radius of a solid NF, and R_{out} and R_{in} are the outer and inner diameter of a hollow NF, respectively. Comparing how well the NF projections fit to the models, one can get some insight into the NF internal structure. The projections were obtained from oxygen STEM/EDX maps by integrating NF segments of length 200 to 800 nm.

To collect structural information about the primary particles, the GPA of lattice fringes proposed by Hÿtch[93] was applied to HRTEM images. In brief, the HRTEM image was Fourier transformed (FT), and the peaks were assigned to the reciprocal vectors $\mathbf{g}_{hkl}$ of the spinel lattice. For each peak of interest, the 2D FT image was filtered by an isotropic Gaussian filter and inverse FT-ed to real space as a complex image. The intensity ($Re^2 + Im^2$) image highlights the regions of the HRTEM image where the $\mathbf{g}_{hkl}$ fringes are present. The phase of the complex image was further processed following ref. [94] to produce the lattice rotation and Lagrange strain maps, corresponding to $\mathbf{g}_{hkl}$. The GPA results are presented in two separate images: i) the fringe-intensity-colored TEM image, i.e., the original black-and-white HRTEM image colorized with yellow hue proportional to the lattice fringe amplitude and ii) the Lagrange strain map, expressed as percentage deviation of the imaged interplanar distance from $1/|\mathbf{g}_{hkl}|$. The rotation maps, expressing the lattice rotation in degree from $\mathbf{g}_{hkl}$ were also calculated to ascertain the single- or poly-crystalline nature of the grains.

In our previous studies,[28] hollow NFs (diameter 100–300 nm) comprised grains with size of several tens of nm, so it was relatively easy to single out individual grains in HR-TEM images and analyze their lattice fringes. In the present case, due to the small size of the grains and the solid (or slightly hollow) morphology of the NFs, it is difficult to individuate the boundaries of individual grains because there is extensive grain overlap in the images. Consequently, it is also difficult to assess the single- or poly-crystalline nature of the grains and their lattice features. Therefore, the usual GPA of lattice fringes could be carried out only for particles at the edge of the NFs.

To recover more information from the HRTEM images, a new analysis mode was introduced where all crystallites with the *same fringe period* in an image are simultaneously imaged. This requires using a Gaussian semicircular mask to filter the 2D FT image to retain all peaks with equal $|\mathbf{g}_{hkl}|$and different lattice orientation. The mask is semicircular (as opposed to circular) to avoid introduction of cosine-oscillations in the real-space final images and Gaussian to dampen the oscillation induced by a step function; unfortunately, Bessel-function oscillations related to the FT of any function depending on $|\mathbf{g}_{hkl}|$ only do show up in the inverse FT-ed real space images. In the final images, crystallites appear as colored patches with hue denoting the orientation of $\mathbf{g}_{hkl}$ in the image plane. In this way, geometrical relationship between crystallites can be investigated and crystallite size can be estimated. No information about crystallite strain can be recovered in this analysis mode. Indeed, the cubic spinel lattice of the crystallites produces HRTEM fringes for a few $\mathbf{g}_{hkl}$, namely <111>, <200>, <220>, and <311>. These $\mathbf{g}_{hkl}$ vectors have low, simple *hkl* indices and the equivalent directions, e.g., [200], [−200], [020], etc. form large angles. For instance, <111> equivalent directions form angles of 70.5° and 109.5°, whereas <200> equivalent directions only form angles of 90°. Inspecting rotation maps of $\mathbf{g}_{hkl}$, it may happen that two neighboring crystallites display *hkl* fringes. If the color assigned to those crystallites in the rotation map is identical (same direction) or correspond to rotation angles equal to one of the angles between equivalent directions, then there may be a crystallographic lattice relationship between the two crystallites. Otherwise, no crystallographic lattice relationship is observed, which, however, is not conclusive proof that such a relationship does not exist. The same applies to the comparison of rotation maps for the same NP region related to different $\mathbf{g}_{hkl}$ vectors.

XRD patterns were recorded with a Bruker D2 diffractometer using Ni β-filtered Cu-K_α radiation source ($\lambda = 0.1541$ nm). Raman scattering was measured by a NTEGRA—Spectra SPM NT-MDT confocal microscope coupled to a solid-state laser operating at 2.33 eV (532 nm) and delivering a power of 250 μW at the sample surface. The scattered light from the sample, collected by a 100X Mitutoyo objective (NA = 0.75), was dispersed by an 1800 lines mm^{-1} grating and detected by a cooled ANDOR iDus CCD Camera. XPS studies were performed on a near-ambient pressure EnviroESCA instrument from SPECS, using an AlKα excitation source ($h\upsilon$ = 1486.6 eV) and working at an operating pressure of ≈10^{-6} mbar. Survey spectra were acquired in the binding energy (BE) range between 0 and 1460 eV, collecting data at 100 eV pass energy, 1.0 eV $step^{-1}$, and 0.1 sec $step^{-1}$. High resolution scans were acquired at 50 eV pass energy, 0.1 eV $step^{-1}$, and 0.1 s $step^{-1}$. XPS curves (BE uncertainty = ± 0.2 eV) were fitted using the Keystone software of SPECS and applying a Shirley-type background function.[95] The sensitivity factors of integrated peak areas used for atomic percentages (at. %) quantification were supplied by SPECS. Further details on the instrumentation can be found elsewhere.[28,96]

Electrochemical Characterization: Electrochemical measurements were performed at RT using a potentiostat/galvanostat workstation (AUTOLAB PGSTAT 204 instruments) and NOVA 2.1.5 software. A three-electrode set-up was used for this purpose with a platinum auxiliary (www.metrohm.com) counter electrode, an Ag/AgCl (www.metrohm.com) reference electrode and a catalyst-loaded screen-printed carbon electrode (SPCE, www.dropsens.com) acting as the working electrode. The OER catalyst solutions were prepared by mixing the catalysts (5 mg) with 5 wt.% Nafion solution (50 μL) and isopropanol (950 μL). KOH (1 M) in demineralized water (pH ≈13.77) was used as the electrolyte. The catalysts were loaded onto the working area (4 mm in diameter) of SPCE; external reference- and counter-electrodes completed the circuit.

As usual,[32,97,98] Nernst equation,

$$E_{RHE} = E_{Ag/AgCl} + 0.0592\ pH + E^0_{Ag/AgCl}\ (\text{with } E^0_{Ag/AgCl} = 0.198\ V \text{ and } pH \approx 13.77 \text{ for 1 M KOH}) \quad (3)$$

was used to convert the measured potentials, $E_{Ag/AgCl}$, into those referred to the reversible hydrogen electrode (RHE), E_{RHE}. Then, the overpotentials for the OER, η_{OER}, were calculated as:

$$\eta_{OER} = E_{RHE} - 1.23V \quad (4)$$

The polarization curves for OER were recorded in LSV mode and at a scan rate of 5 mV s^{-1}. The charge transfer resistance at the electrolyte/electrode interface was determined from the Nyquist plot recorded by conducting electrochemical impedance spectroscopy (EIS) in the frequency range from 1 Hz to 100 kHz at an applied potential of 1.7 V (vs. RHE). Sinusoidal alternating voltages with an amplitude of 0.01 V (V_{rms}) were used.

Experimentally measured potentials (vs. Ag/AgCl) were corrected for the ohmic drop corresponding to the uncompensated solution resistance (R_u). The R_u value was extracted from Nyquist plots of EIS experiments.

The electrochemical measurements for calculating TOF and O_2 production rate were carried out in a lab scale OER reactor with a three-electrode cell equipped with working, reference Ag/AgCl (3 M KCl) and counter Pt electrodes, immersed in an aqueous solution of KOH 1 M under an applied overpotential η of 360 mV. Working electrode (area 1 cm^2) was modified printing 0.9 mg of the CoNi-500 sample. As in a previous paper,[23] turnover frequency (TOF) value for CoNi-500 was calculated by assuming that every metal atom is involved in the catalysis process. The TOF = $jS/4Fn$, where j (mA cm^{-2}) is the measured current density at η = 360 mV (overpotential at 10 mA cm^{-2}), S is the electrode surface area, the constant 4 means 4 electrons/mol of O_2, F is the Faraday´s constant (96 485.3 C mol^{-1}), and n is the mole of the coated metal atoms on the electrode.

Supporting Information

Supporting Information is available from the Wiley Online Library or from the author.

Acknowledgements

C.T. and K.M. contributed equally to this work. Christoph Erdmann was acknowledged for electron microscopy measurements.

Conflict of Interest

The authors declare no conflict of interest.

Data Availability Statement

The data that support the findings of this study are available from the corresponding author upon reasonable request.

Keywords

electrocatalysts, high-entropy spinel oxides, hydrogen production, nanofibers, OER

Received: June 6, 2023
Revised: October 9, 2023
Published online:

[1] L. Osmieri, Y. He, H. T. Chung, G. McCool, B. Zulevi, D. A. Cullen, P. Zelenay, *J. Power Sources* **2023**, *556*, 232484.
[2] J. E. Lee, K-J. Jeon, P. L. Show, I. H. Lee, S.-C. Jung, Y. J. Choi, G. H. Rhee, K-Y. A. Lin, Y.-K. Park, *Fuel* **2022**, *308*, 122048.
[3] S. Wang, A. Lu, C.-J. Zhong, *Nano Converg.* **2021**, *8*, 4.
[4] M. Ji, J. Wang, *Int. J. Hydrog. Energy* **2021**, *46*, 38612.
[5] J. N. Hansen, H. Prats, K. K. Toudahl, N. Mørch Secher, K. Chan, J. Kibsgaard, I. Chorkendorff, *ACS Energy Lett.* **2021**, *6*, 1175.
[6] M. Plevová, J. Hnát, K. Bouzek, *J. Power Sources* **2021**, *507*, 230072.
[7] S M. El-Refaei, P A. Russo, N. Pinna, *ACS Appl. Mater. Interfaces* **2021**, *13*, 22077.
[8] S. Zhang, X. Zhang, Y. Rui, R. Wang, X. Li, *Green Energy .Environ* **2021**, *6*, 458.
[9] F. Song, L. Bai, A. Moysiadou, S. Lee, C. Hu, L. Liardet, X. Hu, *J. Am. Chem. Soc.* **2018**, *140*, 7748.
[10] H. Jing, P. Zhu, X. Zheng, Z. Zhang, D. Wang, Y. Li, *Adv. Powder Mater.* **2022**, *1*, 100013.
[11] C. Zheng, X. Zhang, Z. Zhou, Z. Hu, *eScience* **2022**, *2*, 219.
[12] D. Zhang, Y. Wang, Y. Peng, Y. Luo, T. Liu, W. He, F. Chen, M. Ding, *Adv. Powder Mater.* **2023**, *2*, 100129.
[13] C. Meng, Y. Cao, Y. Luo, F. Zhang, Q. Kong, A. A. Alshehri, K. A. Alzahrani, T. Li, Q. Liu, X. Sun, *Inorg. Chem. Front.* **2021**, *8*, 3007.
[14] F. Gao, J. He, H. Wang, J. Lin, R. Chen, K. Yi, F. Huang, Z. Lin, M. Wang, *Nano Res. Energy* **2022**, *1*, e9120029.
[15] Y. Qiu, Z. Liu, A. Sun, X. Zhang, X. Ji, J. Liu, *ACS Sustainable Chem. Eng.* **2022**, *10*, 16417.
[16] W. Wang, Z. Wang, Y. Hu, Y. Liu, S. Chen, *EScience* **2022**, *2*, 438.
[17] L. Zhang, J. Liang, L. Yue, K. Dong, J. Li, D. Zhao, Z. Li, S. Sun, Y. Luo, Q. Liu, G. Cui, A. Ali Alshehri, X. Guo, X. Sun, *Nano Research Energy* **2022**, *1*, e9120028.
[18] L. Zhang, L. Li, J. Liang, X. Fan, X. He, J. Chen, J. Li, Z. Li, Z. Cai, S. Sun, D. Zheng, Y. Luo, H. Yan, Q. Liu, A. A. Alshehri, X. Guo, X. Sun, B. Ying, *Inorg. Chem. Front.* **2023**, *10*, 2766.
[19] J. Chen, L. Zhang, J. Li, X. He, Y. Zheng, S. Sun, X. Fang, D. Zheng, Y. Luo, Y. Wang, J. Zhang, L. Xi, Z. Cai, Y. Sun, A. A. Alshehri, Q. Kong, C. Tang, X. Sun, *J. Mater. Chem. A* **2023**, *11*, 1116.
[20] C. Yang, K. Dong, L. Zhang, X. He, J. Chen, S. Sun, M. Yue, H. Zhang, M. Zhang, D. Zheng, Y. Luo, B. Ying, Q. Liu, A M. Asiri, M S. Hamdy, X. Sun, *Inorg. Chem.* **2023**, *62*, 7976.
[21] A. Krishnan, R. Ajay, J. Anakha, U. S. K Namboothiri, *Surf. Interfaces* **2022**, *30*, 101942.
[22] H. Maleki, V. Bertola, *Catal. Sci. Technol.* **2020**, *10*, 3140.
[23] C. Triolo, S. Schweidler, L. Lin, G. Pagot, V. Di Noto, B. Breitung, S. Santangelo, *Energy Adv.* **2023**, *2*, 667.
[24] X. Yang, S. Liping, L. Qiang, H. Lihua, Z. Hui, *J. Mater. Chem. A* **2022**, *10*, 17633.
[25] S. Sun, Y. Sun, Ye Zhou, S. Xi, X. Ren, B. Huang, H. Liao, L. P. Wang, Y. Du, Z. J. Xu, *Angew. Chem.* **2019**, *131*, 6103.
[26] Ye Zhou, S. Sun, C. Wei, Y. Sun, P. Xi, Z. Feng, Z. J. Xu, *Adv. Mater.* **2019**, *31*, 1902509.
[27] S. Wahl, S. M. El-Refaei, A. G. Buzanich, P. Amsalem, K. S. Lee, N. Koch, M. L. Doublet, N. Pinna, *Adv. Energy Mater.* **2019**, *9*, 1900328.
[28] A. Ponti, C. Triolo, B. Petrovičovà, A. M. Ferretti, G. Pagot, W. Xu, V. Di Noto, N. Pinna, S. Santangelo, *Phys. Chem. Chem. Phys.* **2023**, *25*, 2212.
[29] A. Senthamizhan, B. Balusamy, Z. Aytac, T. Uyar, *CrystEngComm* **2016**, *18*, 6341.
[30] Qi Hu, Z. Wang, X. Huang, Y. Qin, H. Yang, X. Ren, Q. Zhang, J. Liu, C. He, *Energy Environ. Sci.* **2020**, *13*, 5097.
[31] F. Liu, M. Yu, X. Chen, J. Li, H. Liu, F. Cheng, *Chinese J. Catal.* **2022**, *43*, 122.
[32] Y. Jia, H. Zhang, T. Gu, Y. Wu, Z. Yang, Y. Shao, H. Zhong, *Chem. Eng. J.* **2023**, *460*, 141829.
[33] J. Bao, X. Zhang, Bo Fan, J. Zhang, M. Zhou, W. Yang, X. Hu, H. Wang, B. Pan, Y. Xie, *Angew. Chem.* **2015**, *127*, 7507.
[34] J. Sun, N. Guo, Z. Shao, K. Huang, Y. Li, F. He, Q. Wang, *Adv. Energy Mater.* **2018**, *8*, 1800980.

[35] M. Li, M. Song, W. Ni, Z. Xiao, Y. Li, J. Jia, S. Wang, Y. Wang, *Chin. Chem. Lett.* **2023**, *34*, 107571.
[36] G. Binitha, M. S. Soumya, A. A. Madhavan, P. Praveen, A. Balakrishnan, K. R. V. Subramanian, M. V. Reddy, S. V. Nair, A. S. Nair, N. Sivakumar, *J. Mater. Chem. A* **2013**, *1*, 11698.
[37] M. Fiore, G. Longoni, S. Santangelo, F. Pantò, S. Stelitano, P. Frontera, P. Antonucci, R. Ruffo, *Electrochim. Acta* **2018**, *269*, 367.
[38] Y. Li, H. Zhang, X. Zhang, L. Wei, Y. Zhang, G. Hai, Y. Sun, *J. Mater. Sci.: Mater. Electron.* **2019**, *30*, 15734.
[39] F. Pantò, Z. Dahrouch, A. Saha, S. Patanè, S. Santangelo, C. Triolo, *Appl. Surf. Sci.* **2021**, *557*, 149830.
[40] D. Hu, R. Wang, P. Du, G. Li, Y. Wang, D. Fan, X. Pan, *Ceram. Int.* **2022**, *48*, 6549.
[41] X. Yin, J. Huang, Z. Pu, J. Li, H. Feng, X. Wang, Y. Wang, *Ceram. Int.* **2021**, *47*, 17167.
[42] C. Wei, Z. Feng, G. G. Scherer, J. Barber, Y. Shao-Horn, Z. J. Xu, *Adv. Mater.* **2017**, *29*, 1606800.
[43] S. W. Oh, H. J. Bang, Y. C. Bae, Y.-K. Sun, *J. Power Sources* **2007**, *173*, 502.
[44] J. Dabrowa, M. Stygar, A. Mikula, A. Knapik, K. Mroczka, W. Tejchman, M. Danielewski, M. Martin, *Mater. Lett.* **2018**, *216*, 32.
[45] A. Mao, F. Quan, H.-Z. Xiang, Z.-G. Zhang, K. Kuramoto, A.-L. Xia, *J. Mol. Struct.* **2019**, *1194*, 11.
[46] T. X. Nguyen, J. Patra, J.-K. Chang, J.-M. Ting, *J. Mater. Chem. A* **2020**, *8*, 18963.
[47] D. Wang, S. Jiang, C. Duan, J. Mao, Y. Dong, K. Dong, Z. Wang, S. Luo, Y. Liu, X. Qi, *J. Alloys Compd.* **2020**, *844*, 156158.
[48] H. Chen, N. Qiu, B. Wu, Z. Yang, S. Sun, Y. Wang, *RSC Adv.* **2020**, *10*, 9736.
[49] M. Stygar, J. Dabrowa, M. Mozdzierz, M. Zajusz, W. Skubida, K. Mroczka, K. Berent, K. Swierczek, M. Danielewski, *J. Eur. Cer. Soc.* **2020**, *40*, 1644.
[50] B. Liang, Y. Ai, Y. Wang, C. Liu, S. Ouyang, M. Liu, *Materials* **2020**, *13*, 5798.
[51] Z. Sun, Y. Zhao, C. Sun, Q. Ni, C. Wang, H. Jin, *Chem Eng. J.* **2022**, *431*, 133448.
[52] T. Tangcharoen, J. T-Thienprasert, C. Kongmark, *J. Adv. Ceram.* **2019**, *8*, 352.
[53] B. Purnama, A. T. Wijayanta, Suharyana, *J. King Saud Univ. Sci.* **2019**, *31*, 956.
[54] H. D. Lutz, B. Müller, H. J. Steiner, *J. Solid St. Chem.* **1991**, *90*, 54.
[55] Z. Wang, R. T. Downs, V. Pischedda, R. Shetty, S. K. Saxena, C. S. Zha, Y. S. Zhao, D. Schiferl, A. Waskowska, *Phys. Rev. B* **2003**, *68*, 094101.
[56] V. D'ippolito, G B. Andreozzi, D. Bersani, P. P. Lottici, *J. Raman Spectrosc.* **2015**, *46*, 1255.
[57] P. Choudhary, D. Varshney, *Mater. Res. Express* **2017**, *4*, 076110.
[58] B. Nandan, M. C. Bhatnagar, S. C. Kashyap, *J. Phys. Chem. Solids* **2019**, *129*, 298.
[59] M. A. Laguna-Bercero, M. L. Sanjuán, R. I. Merino, *J. Phys.: Cond. Matter* **2007**, *19*, 186217.
[60] Z. Z. Lazarevic, C. Jovalekic, A. Milutinovic, D. Sekulic, V. N. Ivanovski, A. Recnik, B. Cekic, N. Z. Romcevic, *J. Appl. Phys.* **2013**, *113*, 187221.
[61] M. H. Abdellatif, A. A. Azab, M. Salerno, *Mater. Res. Bull.* **2018**, *97*, 260.
[62] S. Supriya, S. Kumar, M. Kar, *J. Electronic Mater.* **2019**, *48*, 3612.
[63] R. S. Yadav, I. Kuřitka, J. Vilcakova, J. Havlica, J. Masilko, L. Kalina, J. Tkacz, J. Švec, V. Enev, M. Hajdúchová, *Adv. Nat. Sci.: Nanosci. Nanotechnol.* **2017**, *8*, 045002.
[64] W. Wang, Z. Ding, X. Zhao, S. Wu, F. Li, M. Yue, J. P. Liu, *J. Appl. Phys.* **2015**, *117*, 17A328.
[65] B. Talluri, K. Yoo, J. Kim, *J. Environ. Chem. Eng.* **2022**, *10*, 106932.
[66] V. Nefedov, D. Gati, B. Dzhurinskii, N. Sergushin, Y. V. Salyn, *Zhurnal Neorganicheskoi Khimii* **1975**, *20*, 2307.
[67] E. Desimoni, C. Malitesta, P. G. Zambonin, J. C. Rivière, *Surf. Interface Anal.* **1988**, *13*, 173.
[68] B. Wichterlová, L. KrajcKová, Z. Tvaruzková, S. Beran, *J. Chem. Soc., Faraday Trans. 1* **1984**, *80*, 2639.
[69] V. I. Nefedov, Y. V. Salyn, G. Leonhardt, R. Scheibe, *J Electron Spectrosc. Relat. Phenomena* **1977**, *10*, 121.
[70] C. P. Li, A. Proctor, D. M. Hercules, *Appl. Spectrosc.* **1984**, *38*, 880.
[71] K. S. Kim, N. Winograd, *Surf. Sci.* **1974**, *43*, 625.
[72] T. J. Chuang, C. R. Brundle, D. W. Rice, *Surf. Sci.* **1976**, *59*, 413.
[73] J. P. Bonnelle, J. Grimblot, A. D'huysser, *J. Electron Spectrosc. Relat. Phenomena* **1975**, *7*, 151.
[74] B. Strohmeier, *J. Catal.* **1984**, *86*, 266.
[75] G. Pagot, M. C. Cassani, F. Gambassi, B. Ballarin, D. Nanni, M. Coi, D. Barreca, E. Boanini, V. Di Noto, *Surf. Sci. Spectra* **2022**, *29*, 024007.
[76] J. Haber, J. Stoch, L. Ungier, *J. Electron Spectrosc. Relat. Phenomena* **1976**, *9*, 459.
[77] B. J. Tan, K J. Klabunde, P. M. A. Sherwood, *J. Am. Chem. Soc.* **1991**, *113*, 855.
[78] T. J. Frankcombe, Y. Liu, *Chem. Mater.* **2023**, *35*, 5468.
[79] L. Bigiani, A. Gasparotto, G. Carraro, C. Maccato, D. Barreca, *Surf. Sci. Spectra* **2018**, *25*, 024005.
[80] B. Issa, I. M. Obaidat, B. A. Albiss, Y. Haik, *Int. J. Molec. Sci.* **2013**, *14*, 21266.
[81] P. M. Gómez-Largo, C. D. Miranda, A. C. Villagrán-Olivares, C. A. López, B. P. Barbero, *Mol. Catal.* **2022**, *530*, 112639.
[82] X. Duan, M. Pan, F. Yu, D. Yuan, *J. Alloys Compd.* **2011**, *509*, 1079.
[83] A. Sarkar, B. Eggert, R. Witte, J. Lill, L. Velasco, Q. Wang, J. Sonar, K. Ollefs, S. S. Bhattacharya, R. A. Brand, H. Wende, F. M. F. de Grot, O. Clemens, H. Hahn, R. Kruk, *Acta Mater.* **2022**, *226*, 117581.
[84] S. Jiang, K. Tian, X. Li, C. Duan, D. Wang, Z. Wang, H. Sun, R. Zheng, Y. Liu, *J. Colloid Interf. Sci.* **2022**, *606*, 635.
[85] J. Tang, J. L. Xu, Z. G. Ye, X. B. Li, J. M. Luo, *J. Mater. Sci. Technol.* **2021**, *79*, 171.
[86] M. Harada, F. Kotegawa, M. Kuwa, *ACS Appl. Energy Mater.* **2022**, *5*, 278.
[87] H. Chen, L. Shi, X. Liang, L. Wang, T. Asefa, X. Zou, *Angew. Chem.* **2020**, *59*, 19654.
[88] Y. Sun, H. Liao, J. Wang, Bo Chen, S. Sun, S. J. H. Ong, S. Xi, C. Diao, Y. Du, J.-O. Wang, M. B. H. Breese, S. Li, H. Zhang, Z. J. Xu, *Nat. Catal.* **2020**, *3*, 554.
[89] F. Calle-Vallejo, N. G. Inoglu, H. Y. Su, J. I. Martinez, I. C. Man, M. T. Koper, J. R. Kitchin, J. Rossmeisl, *Chem. Sci.* **2013**, *4*, 1245.
[90] S. A. Patil, S. Cho, Y. Jo, N. K. Shrestha, H. Kim, H. Im, *Chem. Eng. J.* **2021**, *426*, 130773.
[91] R. Eppstein, M. Caspary Toroker, *ACS Mater. Au* **2022**, *2*, 269.
[92] S. Nandi, S. K. Singh, D. Mullangi, R. Illathvalappil, L. George, C. P. Vinod, S. Kurungot, R. Vaidhyanathan, *Adv. Energy Mater.* **2016**, *6*, 1601189.
[93] M. J. Hytch, *Microsc. Microanal. Microst.* **1997**, *8*, 41.
[94] J. L. Rouvière, E. Sarigiannidou, *Ultramicroscopy* **2005**, *106*, 1.
[95] D. A. Shirley, *Phys. Rev. B* **1972**, *5*, 4709.
[96] C. Triolo, W. Xu, B. Petrovicovà, N. Pinna, S. Santangelo, *Adv. Funct. Mater.* **2022**, *32*, 2202892.
[97] S.-Q. Chang, C.-C. Cheng, P.-Y. Cheng, C.-L. Huang, S.-Y. Lu, *Chem. Eng. J.* **2022**, *446*, 137452.
[98] L. Danyang, S. Liping, Li Qiang, X. Tian, H. Lihua, Z. Hui, *J. Alloys Compd.* **2022**, *913*, 165148.